Damage Analysis and Close-Range Radar Observations of the 13 April 2019 Greenwood Springs, Mississippi, Tornado during VORTEX-SE Meso18-19

ANTHONY W. LYZA,[a,b] BARRETT T. GOUDEAU,[c] AND KEVIN R. KNUPP[c]

[a] *Cooperative Institute for Severe and High-Impact Weather Research and Operations, University of Oklahoma, Norman, Oklahoma*
[b] *NOAA/OAR/National Severe Storms Laboratory, Norman, Oklahoma*
[c] *Department of Atmospheric and Earth Science, Severe Weather Institute–Radar and Lightning Laboratories (SWIRLL), University of Alabama in Huntsville, Huntsville, Alabama*

ABSTRACT: A tornado outbreak occurred across the Southeast United States on 13–14 April 2019, during the Verification of the Origins of Rotation in Tornadoes Experiment–Southeast (VORTEX-SE) Meso18-19 experiment. Among the most noteworthy events was a pair of large tornadoes in Monroe County, Mississippi, near the Columbus Air Force Base (GWX) Weather Surveillance Radar–1988 Doppler (WSR-88D). The second tornado, near the Greenwood Springs community, formed within the "no data" region near the radar and passed about 900 m to its east, rapidly strengthening into an intense tornado. This tornado produced forest devastation and electrical infrastructure damage up to at least EF4 intensity. The maximum radial velocity from GWX was 81.5 m s^{-1} (182 mph) in a resolution volume centered at 56 m (183 ft) above radar level. This paper presents a damage survey of the Greenwood Springs tornado and compares this assessment to the GWX data. A displacement of the maximum forest damage from the maximum radial velocity, despite the radar beam sampling <100 m ARL, is documented, as well as other likely effects of debris loading by the tornado on the observed radar signatures. The radar observations are placed into context with past mobile radar studies to illustrate the unique nature of this dataset. The relationship between radar data and damage observations, the implications for tornado structure in rough terrain and land cover, and the use of forest damage and radar data in tornado intensity estimation are discussed.

SIGNIFICANCE STATEMENT: This study showcases radar and damage observations of an intense tornado in a forested region of Mississippi. The formation of the tornado within 1 km of a WSR-88D allowed for near-surface radar observations to be collected as significant tree destruction was occurring. Doppler velocities below 60 m above radar level (ARL), near tree canopy top, exceeded 80 m s^{-1}. Tree damage patterns were complicated while the tornado was near maximum intensity. The most severe tree damage was notably displaced from the highest radar-observed velocities, despite the radar sampling as low as 45 m ARL. These findings highlight challenges in utilizing radar data to estimate tornado intensity and structure, particularly in a region of relatively high surface and terrain roughness.

KEYWORDS: Supercells; Tornadoes; Radars/Radar observations; Damage assessment

---

1. Introduction

The Southeast is the most vulnerable region of the United States for tornado impacts, including tornado-related fatalities (Ashley 2007). The region is particularly susceptible to large, long-tracked, significant tornadoes capable of producing widespread damage (Dixon et al. 2011; Coleman and Dixon 2014). Across the Southeast states, 33%–46% of tornadoes occur during the nighttime hours, when residents are more likely to be asleep and less likely to receive advanced warning (Ashley et al. 2008; Kis and Straka 2010; Krocak and Brooks 2018). Mobile and manufactured homes are a common form of housing and are spread across the landscape, leading to increased vulnerability in the Southeast. For example, there is a 350% higher probability of impact to mobile homes in Alabama than in Kansas for any given tornado given the higher mobile home fraction and increased spatial distribution in Alabama (Strader and Ashley 2018).

While many parts of the Southeast feature dense, vulnerable populations, other areas are sparsely populated. Many of these areas are densely wooded and pose challenges to assessing tornado path characteristics, particularly intensity as estimated by the enhanced Fujita (EF) scale. The initial estimation of wind speed values associated with varying degrees of damage to trees was performed through the same process of expert elicitation that was used to develop wind speed estimates for all damage indicators (DIs) and degrees of damage (DODs) in the EF scale (WSEC 2006). None of the experts who participated in the elicitation process were tree damage experts. Recent studies have generally followed two approaches to estimating tornado intensity through tree damage. The first approach employs statistical modeling of wind speed in association with tree-fall fraction in densely forested areas (Godfrey and Peterson 2017). Tree-fall fraction already serves as the underpinning for the tree damage indicator in the Canadian version of the EF scale (Environment Canada 2021). The other primary approaches to estimating tornado intensity from tree damage generally involve fitting a translating Rankine vortex model (Rankine 1901) to observed tree-fall patterns

---

Corresponding author: Anthony W. Lyza, anthony.lyza@noaa.gov

to estimate the corresponding radial, tangential, and total horizontal wind velocity components of the vortex (Holland et al. 2006; Beck and Dotzek 2010; Karstens et al. 2013; Lombardo et al. 2015; Rhee and Lombardo 2018; Rhee et al. 2021). Improving the estimation of tornado intensity through more robust tree damage analysis would serve to improve efforts that are key motivations for tornado intensity estimation in the first place, such as diagnosis of climatological tornado risk (e.g., Feuerstein et al. 2005; Agee and Childs 2014; Lepore and Tippett 2020), understanding the relationship between radar-observed characteristics of tornadic storms and tornado intensity (e.g., LaDue et al. 2012; Van Den Broeke and Jauernic 2014; Kingfield and LaDue 2015; Smith et al. 2015, 2020a,b; Gibbs 2016; Thompson et al. 2017; Gibbs and Bowers 2019), and historical tornado event documentation (e.g., Fuhrmann et al. 2014).

While tree-fall fraction and pattern estimation of tornado intensity are relatively new damage assessment techniques, the evaluation of tree damage from tornadoes is not a novel pursuit. Fujita (1989) utilized tree-fall damage in Grand Teton National Park to estimate the intensity of an extremely large tornado that impacted the area on 21 July 1987, estimating the damage to be of F4 intensity on the legacy Fujita scale. Other notable past tornadoes in densely forested areas have included an F5 tornado in the Bankhead National Forest in northwestern Alabama on 3 April 1974 (Vaughan and Vonnegut 1976), an F4 tornado of greater than 4 km maximum damage width in the Moshannon State Forest of central Pennsylvania on 31 May 1985 (Forbes 1998), and an F3 tornado in the Uinta Mountains of Utah on 11 August 1993 (Dunn and Vasiloff 2001). Additional studies have shown that tree damage from tornadoes can be identified in satellite imagery, either through land cover changes (Jedlovec et al. 2006; Molthan et al. 2014; Kingfield and de Beurs 2017) or direct identification in visible imagery on the order of centimeters of resolution (e.g., Lyza et al. 2019).

The need for estimating tornado intensity from damage arises from the scarcity of direct measurements of tornadoes. In situ measurements of tornadoes are exceedingly uncommon, limited to a select number of targeted observations (e.g., Karstens et al. 2010; Lee et al. 2011; Wurman et al. 2013) or through serendipitous encounters between tornadoes and surface meteorological instruments (e.g., Blair et al. 2008; Blanchard 2013). However, the difficulty and inherent risks associated with the collection of in situ tornado measurements (e.g., Wurman et al. 2014) have led to the use of mobile Doppler radar systems as a preferred method for collecting information about tornado structure. Such studies have elucidated aspects of tornado characteristics and evolution such as genesis and dissipation processes (e.g., Bluestein et al. 2003b, 2016, 2019; Wurman et al. 2007a,b; Atkins et al. 2012; French et al. 2013; Kosiba et al. 2013; Houser et al. 2015; Klees et al. 2016; McKeown et al. 2020), near-surface intensity (e.g., Bluestein and Pazmany 2000; Burgess et al. 2002; Alexander and Wurman 2005; Wurman and Alexander 2005; Tanamachi et al. 2013; Bluestein et al. 2015; Wakimoto et al. 2016; Houser et al. 2020), vortex structure (e.g., Wurman and Gill 2000; Wurman 2002; Bluestein et al. 2003a, 2004, 2007a,b, 2015, 2018, 2019; Alexander and Wurman 2005; Lee and Wurman 2005; Wurman and Alexander 2005;

Tanamachi et al. 2007, 2013; Wurman et al. 2007b, 2010, 2013; Marquis et al. 2008; Wakimoto et al. 2011, 2012, 2018, 2020; Atkins et al. 2012; Kosiba and Wurman 2013; Wurman and Kosiba 2013; French et al. 2014, 2015; Houser et al. 2016; Mahre et al. 2018; Griffin et al. 2019; Wienhoff et al. 2020), and even the confirmation or refutation of tornado existence (e.g., French et al. 2009, Snyder et al. 2020, Wienhoff et al. 2020). These studies, however, nearly ubiquitously examine tornadoes that occurred over the Great Plains region of the United States, where relatively flat, open land provides the most frequent opportunities for the near-range, high-resolution radar data collection necessary to resolve the tornado- and near-tornado-scale circulation. Conversely, while the Southeast is at least as prone to tornadoes as the Plains, the combination of terrain, copious tree coverage, higher population density, and more nocturnal tornado events poses extreme difficulty to obtaining targeted observations of tornadoes with mobile radars. Recent mobile radar observational efforts in the Southeast, in association with the Verification of the Origins of Rotation in Tornadoes Experiment-Southeast (VORTEX-SE) project, have focused on designing radar networks using known, pre-scouted locations to minimize low-level beam blocking of the mobile radar assets (e.g., Lyza et al. 2020b). This prearranged strategy serves to target storm-scale and near-storm environment research goals, with the understanding that acquiring tornado-scale-resolution data would require the serendipity of a tornado passing very close to one of the radar sites comprising the instrumentation domain.

One such serendipitous event occurred late in the evening of 13 April 2019, during the VORTEX-SE Meso18-19 field campaign. A cyclic high-precipitation supercell embedded within a quasi-linear convective system (QLCS) produced a pair of large tornadoes in Monroe County, Mississippi, as part of a regional tornado outbreak (Fig. 1). The second tornado in Monroe County, near Greenwood Springs, formed the "no data" region of the National Weather Service (NWS) Weather Surveillance Radar–1988 Doppler (WSR-88D) that serves nearby Columbus Air Force Base (GWX). The center of the damage track passed approximately 920 m east of the radar site at closest pass, rapidly intensifying into an extremely powerful tornado as it moved away from GWX. Fortuitously, the tornado proceeded to move through a sparsely populated portion of Monroe County, mostly impacting a combination of wooded areas and some harvested plots and only impacting residences along the fringes of the track or well after the tornado had weakened substantially from peak intensity.

The extremely close passage of the Greenwood Springs tornado to the GWX radar allows for the rare opportunity to evaluate the near-surface intensity of a tornado in the Southeast United States and near-surface radar observations in comparison to significant tree devastation. Damage survey and radar data collection and analysis methods are described in detail, and caveats to each are discussed to form a robust understanding of potential error sources. The utility of this dataset to further bolster tree damage assessment using the EF scale is addressed.
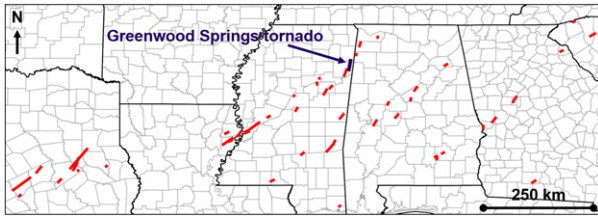
FIG. 1. Overview map of the 13–14 Apr 2019 tornado outbreak across the southern United States. The location of the Greenwood Springs tornado is highlighted in purple, with other tracks in red. Additional tornadoes occurred farther to the north across Ohio and Pennsylvania on the afternoon of 14 Apr (not shown).

2. Data and methods

Monroe County, Mississippi, lies within the NWS Memphis Weather Forecast Office's (WFO MEG) county warning area. WFO MEG dispatched a survey team to the area on 14 April to assess the damage associated with the tornadoes. However, a 14-km portion of the Greenwood Springs track featured no damage information from the original survey team (Fig. 2). Personal communication with meteorologists at WFO MEG indicated that this portion of the track was largely inaccessible on 14 April, owing to tree falls blocking roads that would be needed to access the area.

To better understand the damage caused by the Greenwood Springs tornado, the first two authors (Lyza and Goudeau) performed an additional ground survey of the track 2 days later, on 16 April. This survey focused on the 14-km gap in the original ground survey by WFO MEG. Upon realizing the true scope of the damage in this region (described in section 3) and noting its proximity to GWX, a plan was developed to have aerial imagery collected along the track of the tornado. This imagery was collected on 30 April through SellersPhoto,

a Huntsville-based commercial aerial photography service. A total of twenty-eight 300-megapixel aerial images were collected along the Greenwood Springs tornado track, each with an image resolution of ≈15 cm.

This imagery was then georeferenced in the ArcGIS and QGIS software packages and synthesized with the ground survey information into a final assessment of the tornado track. The intensity assessment was derived strictly from the damage information (i.e., radar data were not used to assign the rating applied to the tornado). To more accurately estimate the intensity of the tree damage produced by the tornado, four adjacent 1800-m-wide cross sections of 100 m × 100 m plots (72 plots total) were drawn across the track in the region of maximum tree fall to apply the tree-fall fraction method for estimating tornado intensity from Godfrey and Peterson (2017). Given the large size of the tornado and local tree farming and harvesting practices, many of the plots did not have uniform mature tree coverage. Additionally, the 15-cm resolution and density of mature trees in the plots that did have full tree coverage made it difficult to identify a precise fraction of tree fall for plots were a large majority (>80%) of trees were either standing or fallen. However, the damage was so severe in the core of the damage track that this method was found to be useful to help apply a maximum damage intensity, in consultation with several tree damage experts, since several plots had no identifiable trees left standing. The Canadian EF scale, which is based in part on the methods of Godfrey and Peterson (2017), was also referenced in assessing the maximum damage intensity. Tree-fall patterns in the peak intensity damage swath were also compared qualitatively to model results from Holland et al. (2006) to bolster confidence in the maximum damage intensity estimate. The final damage assessment is provided in section 3, along with a comparison of this methodology to the operational U.S. EF scale.
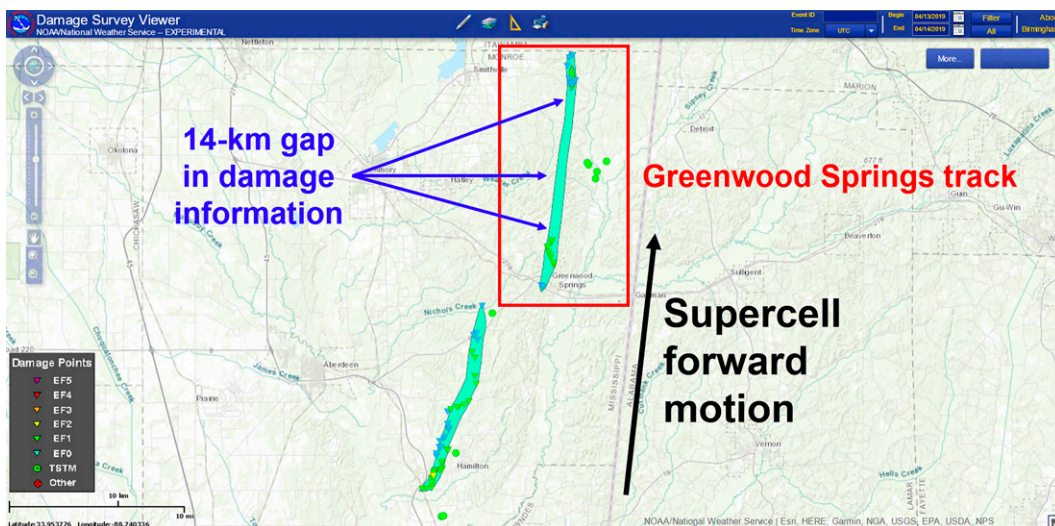

FIG. 2. Screenshot taken from the NWS Damage Assessment Toolkit (DAT) on 26 Apr 2019 of the 13 Apr 2019 Monroe County, Mississippi, tornado tracks, as assessed by WFO MEG. The Greenwood Springs tornado track and the 14-km gap in damage information are highlighted.

FIG. 3. Images of severe tree damage found by the UAH ground survey team along Brown Taylor Road NNE of the GWX radar. (top) What appeared as likely extreme tree damage just west of the road is noted.

Radar data from GWX were also examined to glean further information about characteristics of the Greenwood Springs tornado. GWX was operating in volume coverage pattern (VCP) 212 (NWS 2021) with two additional 0.5° sweeps per volume through the Multiple Elevation Scan Option for Supplemental Adaptive IntraVolume Low-Level Scan (MESO-SAILS; Chrisman 2014) option, resulting in a volume time ranging between 5 min 56 s and 6 min 15 s and 0.5° elevation sweeps ranging from 1 min 49 s to 2 min 13 s during the life cycle of the Greenwood Springs tornado. The proximity of this tornado to GWX posed challenges to automatic de-aliasing of radar data near the time of the tornado's likely peak intensity, despite a Nyquist velocity of 24.1 m s^{-1} at the 0.5°, 0.9°, and 1.3° elevations. Manual de-aliasing of velocity data was performed using the SOLO3 software package from NCAR (Oye et al. 1995). Once de-aliased, the maximum radial velocity and the rotational velocity (V_{ROT}), defined as half the difference between the maximum and minimum radial velocity values, were calculated for each sweep during the tornado's life cycle where the rotational couplet was centered below 1 km above radar level (ARL) as estimated using a calculation of beam height employing the effective Earth radius (e.g., Schelleng et al.

1933). The Python ARM Radar Toolkit (Py-ART; Helmus and Collis 2016) software package was used to plot the radar data.

Characteristics of the polarimetric tornado debris signature (TDS; e.g., Ryzhkov et al. 2005) were also assessed. Since the "best" copolar correlation coefficient (ρ_{hv}) threshold for defining a TDS is unresolved (e.g., Schultz et al. 2012; Bodine et al. 2013; Skow and Cogil 2017), sensitivity tests were carried out to examine how different thresholds would impact the analysis of TDS characteristics with the Greenwood Springs tornado. TDS diameter and depth were evaluated for thresholds of $\rho_{\mathrm{hv}} < 0.80$, 0.85, 0.90, and 0.95. To minimize sensitivity of TDS diameter to the variability of beamwidth at differing ranges, TDS diameter was measured along-radial. The resolution volume range depth of the GWX radar data was 250 m, the beamwidth was 0.9°, and the azimuthal sampling interval (radial increment) was reduced to 0.5° through the employment of super-resolution data processing (Brown et al. 2005; Wood et al. 2009).

3. Damage survey findings

This initial damage survey on 14 April led to WFO MEG assigning the Greenwood Springs tornado a pathlength of 21.2 km (13.2 mi), a path width of 366 m (400 yd), and an EF1 rating, with maximum 3-s gust speed estimated at 42.5–44.7 m s^{-1} (95–100 mph; IEM 2020). The follow-up survey by UAH personnel on 16 April focused on the 14-km gap between damage points in the damage assessment toolkit (DAT) described in section 2. The UAH survey team traveled north to south through the information gap. At the northern end of the gap, the team estimated tree damage at EF1–EF2 intensity across a width of ≈805–965 m (0.5–0.6 mi). The damage indicated the possible presence of multiple vortices within the tornado, with distinct swaths of more intense tree damage embedded within lesser damage. At least one instance of substrate lofting was observed, with about half of a yellow pine tree thrown ≈20 m toward the west, inward toward the center of the tornado track.

The severity and extent of the damage observed by the UAH survey team steadily increased as the team progressed southward along the track. Eventually, tree damage peaked in nearly total annihilation of mature forest, consisting of yellow pine and some hardwood species, along Brown Taylor Road, approximately 3–7 km NNE of GWX. Tree falls along the road traveled by the survey crew were estimated to comprise at least 75% of trees, with evidence of potentially more significant tree-fall fraction closer to the tornado center (Fig. 3). Damage extended along one road roughly normal to the long axis of the path for at least 1600 m (1 mi).

In addition to the tree damage, the survey team encountered crews from the Tennessee Valley Authority (TVA), who were replacing five 500-kV transmission truss towers downed in the tornado. Drone footage acquired by Live Storms Media, Inc.[1] and obtained by the survey team confirmed their collapse. One tower had two of its support footers pulled out of the ground, and another had a portion

---

[1] A watermarked version of the drone footage can be viewed publicly at https://www.youtube.com/watch?v=SpDx_2r6LQ8.
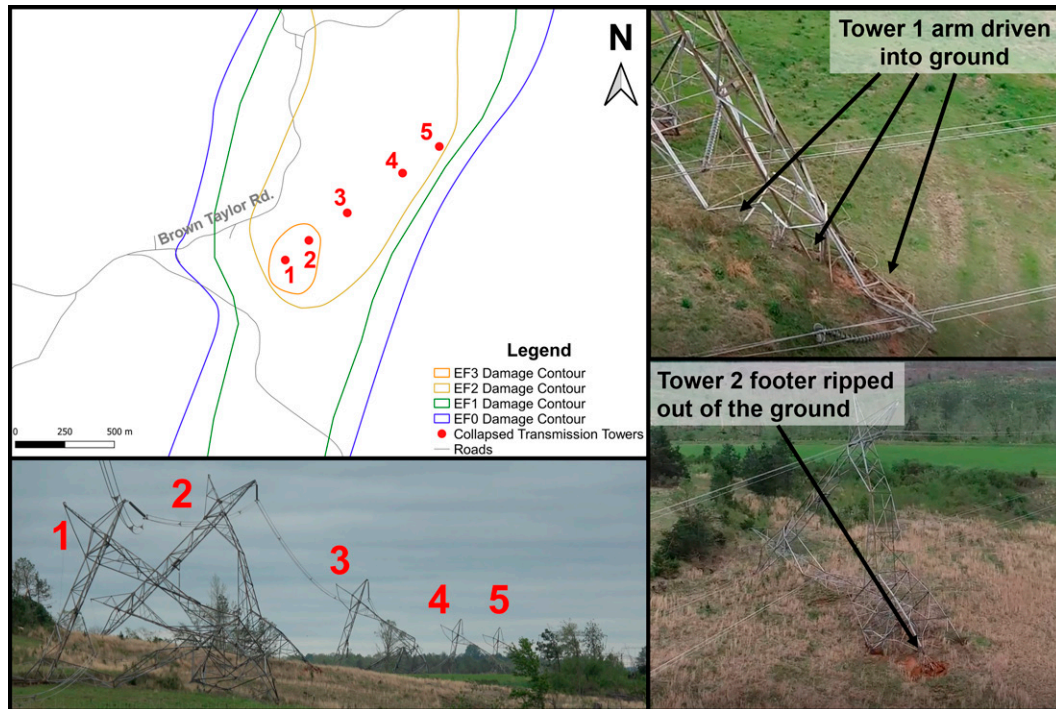
FIG. 4. (top left) Map of the location of downed transmission towers, (bottom left) side-view drone footage of the collapsed towers, and (top right) drone footage of the impaling of one arm of tower 1 into the ground and (bottom right) the loosening of a footer of tower 2 from the ground. The numbers on the map correspond to each of the tower numbers in the image and in the text. Drone footage supplied by Live Storms Media, Inc., and used with permission.

of its arm structure driven into the soil (Fig. 4). The other three towers exhibited somewhat lesser damage to their structures, indicating they may have failed from a combination of wind and stresses applied along the power lines by the other two failed towers. The UAH team assessed the three lesser-damaged towers as EF2, while the two more severely damaged towers were rated EF3. The EF3 rating to the towers was applied based on the damage indicator (DI 24 on the U.S. operational EF scale) and degree of damage (DOD 6) to the towers in the context of the surrounding severe tree damage. Trees near the EF2 towers also suffered lesser damage.

Aside from the damage to the transmission towers, only limited damage to built infrastructure was noted. Most structures impacted by the tornado resided along the outer fringes of the tornado track. A barn was leveled on the western fringe of the tornado track, near the downed transmission towers and estimated area of peak tornado intensity. One of the metal panels from the roof of the barn was discovered by the UAH survey team to have cut through a stand of brush and impaled itself approximately 30 cm (1 ft) into an embankment. Damage to this barn was assessed to be EF2 (DI 1, DOD 8). A couple residential buildings and additional outbuildings nearby received EF0–EF1 damage (DI 1, DOD2; DI 2, DOD 4) along the far western edge of the tornado track.

Most of the other damage to structures caused by this tornado occurred near the end of the tornado track and was assessed to be EF0 damage by WFO MEG. One abandoned frame home was impacted along the eastern fringe of the most intense core of tree damage, just northwest of the collapsed transmission towers. While this structure did survive intact, several large trees were observed to have fallen on it (Fig. 5). The survival of this structure and its implications for interpretation of the intensity of the tornado are discussed in section 5.

While the ground survey provided a wealth of information about the true magnitude of the Greenwood Springs tornado, several questions remained. The survey team could confirm that the total swath of damage was at least 1600 m (1 mi) wide, but there was still substantial uncertainty in the maximum width. This uncertainty was largely driven by an 8-km stretch of the tornado track where no public roads crossed the western edge of the damage swath. Additionally, it was unclear to the survey team whether all the damage observed was due to the tornado itself or if some of it may have been caused by the rear flank downdraft (RFD) outflow of the supercell.

As described in section 2, aerial imagery was obtained by UAH personnel through the SellersPhoto aerial photography company in Huntsville to address these uncertainties. The aerial imagery confirmed the wide extent of tree destruction. It revealed a swath approximately 200–300 m wide of near-100% tree fall just west of the road where the UAH survey team witnessed the most intense tree damage (Fig. 3). The aerial imagery also revealed extensive complexity to the pattern of tree falls at several points along the track. These complexities included

FIG. 5. House with numerous trees fallen onto it just outside the swath of most severe tree damage along Brown Taylor Road.

sharp bifurcations in tree-fall direction and nearly closed circulation patterns of fallen trees (Fig. 6).

One distinct area of divergence in the tree-fall direction was noted along the eastern edge of the damage swath near the area of maximum width, with trees transitioning from falling along the forward motion vector of the tornado to falling outward away from the path of the vortex (Fig. 7). This region of divergent tree-fall orientation indicated that some of the damage around the region of maximum width was likely due to the RFD outflow and not directly caused by the tornado. This RFD outflow damage, consisting of isolated to scattered tree falls toward the east and northeast, as well as more minor tree damage, was found by both the WFO MEG and UAH ground survey teams to the east of the main damage swath, suggesting a local enhancement in the RFD outflow. Radar observations from the GWX radar also support a microburst in the RFD, which is discussed in section 4.

Overall, a synthesis of the ground surveys and aerial photography led to a maximum width estimate of approximately 1890 m (1.17 mi). The aerial imagery also supported an adjustment of the start and end points of the tornado track, with the tornado beginning south of U.S. 278 and ending in far southern Itawamba County, for a total track length of approximately 24.6 km. Assigning a peak damage intensity was challenging. The high-tension tower damage was the most significant damage to built infrastructure, which supported a rating of at least EF3. In the initial analysis of this tornado, the operational EF scale used in the United States was used to assess EF2 damage to trees in the core of the tornado track (Lyza et al. 2020a). However, the American Society of Civil Engineers' (ASCE) Wind Speed Estimation Standards Committee (WSE) has been developing revised tree DIs for the EF scale to more

accurately gauge the intensity of tornado damage to forests (LaDue 2016; LaDue et al. 2018). The revised DIs for tree damage have yet to be finalized as of this writing, but similar to the Canadian EF scale (Environment Canada 2021), one option will likely have a foundation based in the fraction of tree fall observed along the path, as in Godfrey and Peterson (2017; C. Godfrey, J. LaDue, C. Peterson 2019, 2022, personal communication). As discussed in section 2, a series of four adjacent 1800-m-wide cross sections of 100 m × 100 m plots (72 plots total) across a particularly severe swath of tree damage revealed five plots where tree fall appeared to exceed 95% of trees (Fig. 8). Table 1 summarizes the various intensity estimations provided by the U.S. EF scale, the Canadian EF scale, and the Godfrey and Peterson (2017) method for >95% of trees felled within a 100 m × 100 m area.

While a Rankine vortex model method to estimate tornado intensity from the pattern of observed tree fall was not directly applied in this study, a cursory comparison of the patterns evident in Figs. 6 and 8 to simulations presented in Holland et al. (2006, hereafter H06) show similarity to those modeled for loblolly pines in a tornado with a translation speed of 20–30 m s^{-1} and a maximum ground-relative wind speed of 92–102 m s^{-1} (their Figs. 13c,d). There are three key points of comparison between the observed tree-fall patterns in the Greenwood Springs tornado and the H06 simulations:

1) The Greenwood Springs tornado had an estimated forward motion of 24–27 m s^{-1} during its most intense stage, as estimated from GWX observations, 4–7 m s^{-1} faster than the 20 m s^{-1} simulation and 3–6 m s^{-1} slower than the 30 m s^{-1} simulation.

2) More substantial areas of tree fall against the tornado were observed in the Greenwood Springs tornado at peak
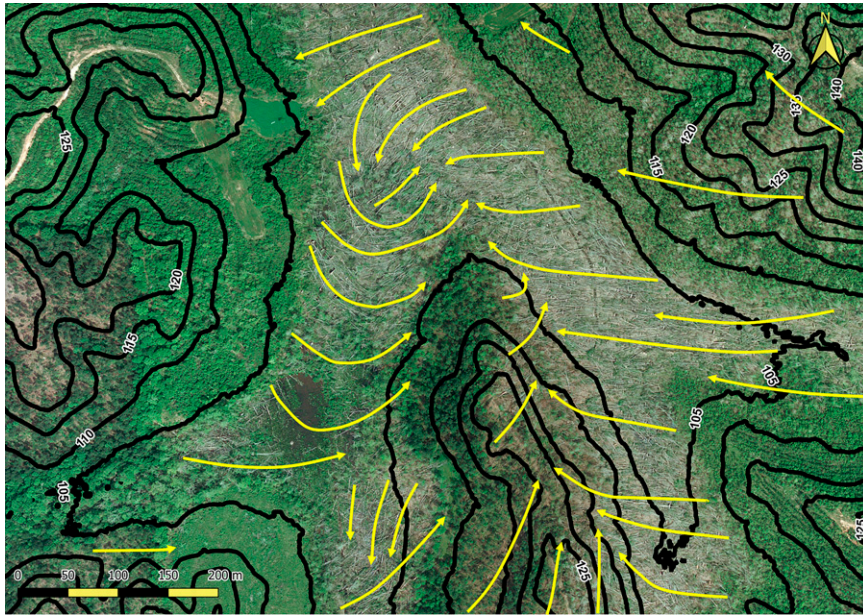
FIG. 6. Example of complicated tree-fall patterns observed in the Greenwood Springs tornado aerial imagery toward the end of the stretch where the tornado was likely at or near peak intensity. Yellow arrows indicate the approximate direction of tree fall, and black contours indicate elevation (m MSL) from a digital elevation model. The tornado was moving approximately from bottom to top of the image with a translation speed estimated at 25 m s^{-1} from GWX observations.

intensity (e.g., Fig. 6) than in the simulations. H06 illustrates how tree fall against the forward motion of a tornado decreases with increasing forward speed for tornadoes of the same ground-relative maximum wind speed (their Figs. 10–12).

3) The swath of maximal tree damage observed in the Greenwood Springs tornado was much larger than in the H06 model simulations (≈100–120 m wide in the H06 Fig. 13c simulations versus >200 m wide at peak intensity in Greenwood Springs).

FIG. 7. Aerial imagery highlighting the likely transition between tornado damage (south–north tree falls on the left) and RFD microburst damage (west–east tree falls on the right) near the area of maximum continuous damage width.
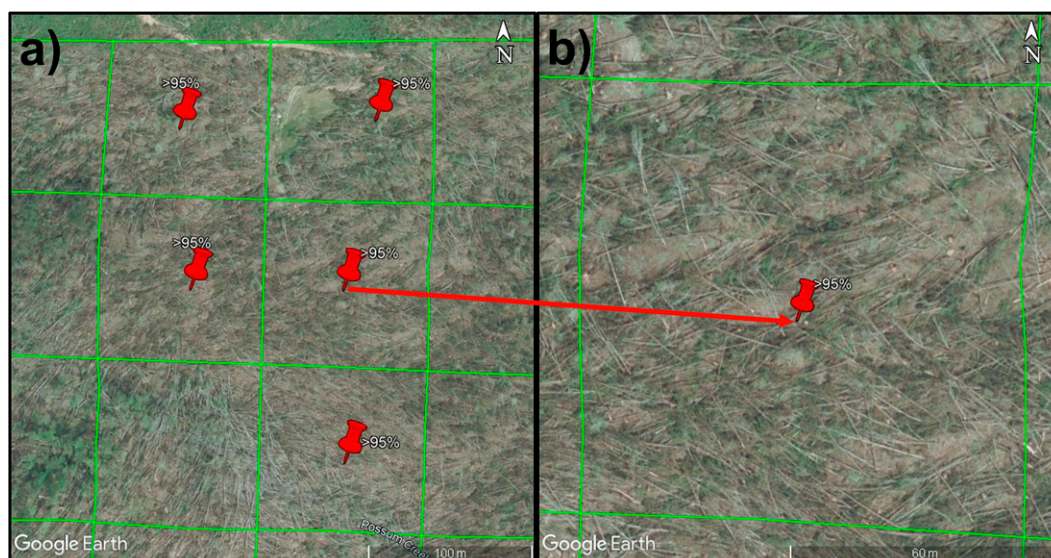
FIG. 8. (a) Overview of the five 100 m × 100 m plots estimated to feature >95% tree fall in the analyzed cross sections of the Greenwood Springs tornado track. (b) Zoomed depiction of the right-center plot (as indicated by the red arrow).

These comparisons point to the *possibility* that the tree damage patterns observed in the Greenwood Springs tornado damage may have been associated with winds exceeding 90–100 m s^{-1}, particularly since loblolly pines, the species modeled in H06, were common along the Greenwood Springs track.

Given the differences between the U.S. EF scale, the Canadian EF scale, and that the tree DIs for the U.S. EF scale are likely to undergo a significant change in the future (which will likely align them closer to the current Canadian EF scale tree DI), the Canadian EF scale and the Godfrey and Peterson (2017) method were used to assign a maximum rating to the most severe tree damage in this study, with the qualitative comparison to the Rankine vortex model in Holland et al. (2006) used as a confidence builder. Additionally, five outside damage survey experts (C. Godfrey, J. LaDue, F. Lombardo, C. Peterson, and Z. Wienhoff 2022, personal communication), including four with specific expertise in tree damage, were consulted in assigning an EF rating to the most severe tree damage. The final estimation of maximum damage intensity based on the available damage indicators was at least EF4,[2] with a maximum 3-s gust exceeding 76.0 m s^{-1} (≥170 mph). Figure 9 summarizes the entire damage track. How this damage assessment compares to the radar observations from GWX and the implications for the EF scale are discussed in section 5.

4. Radar observations

The large size of the Greenwood Springs tornado and its proximity to the GWX WSR-88D afforded an opportunity to coarsely resolve the tornado structure as low as 47 m ARL as

it was producing the peak intensity damage observed in the damage analysis. The western edge of the tornado was approximately 700 m away from GWX at closest approach, with the center of the damage track about 920 m away. The close approach to GWX provided radar sampling nearly parallel to the forward motion vector of the tornado, leading to GWX sampling nearly the maximum ground-relative wind component despite a translational speed of between 20 and 27 m s^{-1}. Figure 10 details the maximum Doppler velocity (V_{max}) and V_{ROT} for all sweeps where the couplet associated with the tornado was centered ≤200 m above radar level (ARL).

The most intense V_{max} value recorded by the GWX radar was 81.5 m s^{-1} (182 mph) at 56 m (183 ft) ARL at 0425:51 UTC (Fig. 11), at an elevation angle of 0.9° and a range of 3.62 km.[3] At the lowest elevation scan with a reliable sampling of the tornado cyclone, GWX detected a V_{max} of 76.0 m s^{-1} (170 mph) at 47 m (154 ft) ARL at 0427:16 UTC, at an elevation angle of 0.5° and a range of 5.62 km. The peak observed V_{ROT} value was 50.3 m s^{-1}, coincident with peak V_{max} measurement at 0425:51 UTC. The V_{max} and V_{ROT} remained >70 and 40 m s^{-1}, respectively, until 0431:22 UTC, when both values began to steadily decrease prior to tornado dissipation (around 0440 UTC).

The TDS associated with the Greenwood Springs tornado was large as soon as it moved out of the "no data" region of the GWX radar. The very first sweep where the TDS diameter could be confidently determined (the 0.9° sweep at 0425 UTC where the 81.5 m s^{-1} V_{max} was detected in Fig. 10) featured a maximum TDS radial diameter of 1.75 km, using a

---

[2] This analysis is independent of WFO MEG's final assessment of EF2 damage intensity in *Storm Data*.

---

[3] The 81.5 m s^{-1} value represents a "best interpretation" through manual de-aliasing of the GWX radar data. Given the subjective nature of manual de-aliasing, it is worth noting that some potential for error exists in interpretation of these precise values.

TABLE 1. Summary of applicable tree damage assessment methods from the operational U.S. EF scale, the operational Canadian EF scale, and from the methodology in Godfrey and Peterson (2017). For the U.S. and Canadian EF scales, the three numbers provided for the estimated wind speed range represent the lower-bound, expected, and upper-bound 3-s, 10 m AGL maximum wind gust values for each damage indicator (DI), degree of damage (DOD) combination.

Damage assessment method	Maximum-applicable tree DI, DOD	Estimated wind speed range (m s^{-1})	Possible EF rating range
Operational U.S. EF scale (WSEC 2006)	DI 27 ("Trees: Hardwood"), DOD 6 ("Trunks snapped")	41.6–49.2–59.9	EF1–EF2
Canadian EF scale	Chapter 27 ["C-2 Trees (C-T)"], DOD 6 ("More than 80% of mature trees snapped and/or uprooted; numerous trees may be denuded/debarked by missiles with only stubs of largest branches remaining")	52.8–65.3–76.4	EF2–EF4
Godfrey and Peterson (2017)	>95% of trees felled in a 100 m × 100 m plot	≥80 [5]	EF4–EF5

threshold of $\rho_{hv} < 0.8$. The maximum TDS diameter using the $\rho_{hv} < 0.8$ threshold was 3.00 km, achieved on two 0.5° sweeps at 0431:04 and 0434:57 UTC and a 5.1° sweep at 0434:42 UTC, and the maximum depth was approximately 4.81 km (15.8 kft) on the 0431:04–0436:47 UTC GWX volume.

The sensitivity tests using ρ_{hv} thresholds of $\rho_{hv} < 0.80$, 0.85, 0.90, and 0.95 revealed that TDS diameter was sensitive to the choice of threshold. The maximum TDS diameters for each threshold were 3.00, 4.75, 7.00, and 10.25 km, respectively. The 3.00-km maximum diameter at the most restrictive threshold of $\rho_{hv} < 0.80$ would place it near the upper echelon of TDS diameters catalogued in Schultz et al. (2012),[4] particularly for tornadoes in close range to the sampling radar. Maximum TDS depth was less sensitive to the choice of threshold, with maximum depths of 4.81, 4.81, 4.92, and 4.92 km, respectively. These TDS depths all exceed the average values for maximum TDS vertical extent for EF3–EF4 tornadoes found in Van Den Broeke and Jauernic (2014, their Table 2) and far exceed the average values for maximum TDS vertical extent observed in either coniferous or deciduous forests in tornadoes rated ≥EF2 (Van Den Broeke and Jauernic 2014, their Fig. 7b). Time–height plots of TDS radial diameter for each threshold indicate that maximum diameter was generally located higher in elevation and later in time for progressively less restrictive ρ_{hv} criteria (Fig. 12). It is hypothesized that this pattern is due to the centrifuging and dispersion of lofted debris leading to wider expanses of lesser amounts of debris being sampled by the radar beam up to higher elevations later in the life cycle of the tornado. This dispersion of debris, like that documented in Van Den Broeke (2015), can clearly be seen in plan position indicator (PPI) scans from GWX (Fig. 13).

As the Greenwood Springs tornado moved away from GWX, a microburst was observed between the tornado and the dissipating initial tornado, within the rear-flank downdraft of the storm (Fig. 14). Evidence of this microburst was also found in the ground damage surveys by both UAH and WFO MEG, as described in section 3. The RFD microburst immediately preceded the beginning of a weakening trend in both V_{max} and V_{ROT} that persisted through the dissipation of the tornado.

5. Discussion

The damage survey, aerial photography, and GWX radar observations all indicate that the Greenwood Springs tornado was a violent event. The proximity of the most intense damage to the GWX radar allowed for a unique opportunity to compare the observed damage to radar observations in a heavily wooded area. Furthermore, this case presents a rare opportunity to capture the near-maximum wind velocity component of a fast-translating tornado given its motion nearly parallel to radials from GWX.

As shown in Fig. 10, there were six sweeps where GWX recorded V_{max} values that exceeded 60.8 m s^{-1} (136 mph), the lower-bound wind speed for the EF3 range on the EF scale, below a height of 200 m ARL. Three sweeps featured V_{max} values that exceed 74.0 m s^{-1} (166 mph), the lower-bound wind speed for the EF4 range. In two of these sweeps, the V_{max} values were below 60 m ARL. There are, however, several caveats in relating these radar measurements to the observed damage along the track and are described below for this case. These caveats are similar to those for using mobile radars to estimate tornado intensity that are described in Snyder and Bluestein (2014). Additionally, given the ongoing assessment of the use of radar in evaluating tornado intensity, it is worthwhile to assess the GWX observations in comparison with observations of tornadoes from mobile radars.

---

[4] Schultz et al. (2012) used a threshold of $\rho_{hv} \leq 0.70$ to define a TDS to more confidently discriminate between debris and hail using a C-band radar.
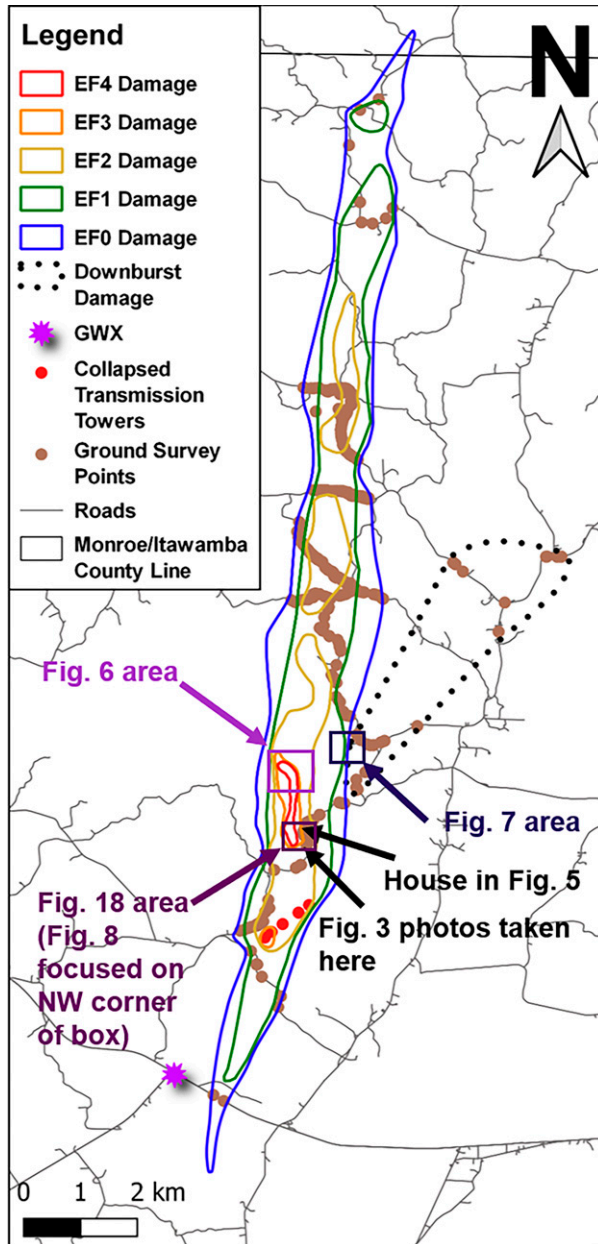
FIG. 9. Overview map of the Greenwood Springs tornado track, synthesizing information from the UAH and WFO MEG ground damage surveys and aerial photography. The locations of damage showcased in figures elsewhere in this manuscript are annotated.

The EF scale wind speed estimates are calibrated as 3-s gusts at 10 m above ground level (AGL; Snyder and Bluestein 2014). While the radar measurements presented are at very

[5] The Godfrey and Peterson (2017) estimated wind speed range minimum value was approximated by their Fig. 7, estimating the lower-bound threshold of the 95% confidence interval for the wind speed necessary to fell >95% of trees in a 100 m × 100 m plot.
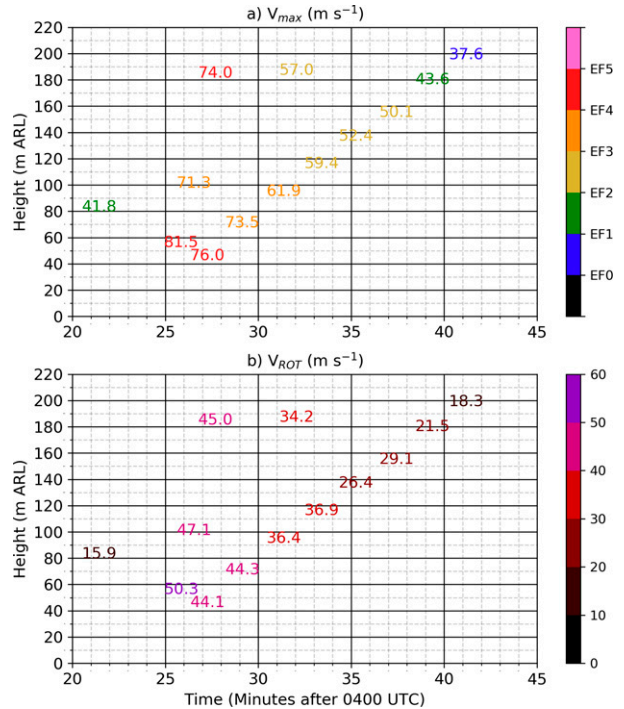
FIG. 10. Time–height depictions of (a) maximum Doppler velocity (V_{max}) and (b) rotational velocity (V_{ROT}) below 200 m ARL for the Greenwood Springs tornado from the GWX radar. The V_{max} values are shaded by the EF wind gust range into which they would fall if they represented a 3-s, 10 m AGL gust value, as indicated by the color bar.

low elevations relative to ground level compared to the vast majority of serendipitously collected radar data of tornadoes, how they relate to elevations above ground level can vary substantially from the radar elevation reference point. The GWX radar is located atop a local high point in land elevation, with a land elevation of approximately 148 m above mean sea level (MSL). With a 21 m (70 ft) tower, the elevation of the antenna is approximately 169 m MSL. The land elevation along the Greenwood Springs tornado track generally increases from the start of the track to the end of the track, ranging from approximately 100 to 170 m MSL.

However, as suggested by the elevation of GWX despite it being located near the start of the track, the land elevation varies substantially along the track. These variations can be as substantial as 20–40 m over relatively short distances (e.g., Fig. 6). With a resolution volume range depth of 250 m, some of these variations can occur within the distance of a single sample volume gate of the GWX radar, indicating that the height above ground level that a given radar gate represents can vary substantially within the area of a given gate, let alone across adjacent gates.

Such changes in land elevation within a radar gate area are likely critical to relating how the measured Doppler velocity compares to the true intensity of the tornado according to the EF scale gust standard. Analysis of 12 volumes of Rapid-Scan Doppler-On-Wheels (RSDOW) data from the 25 May 2012
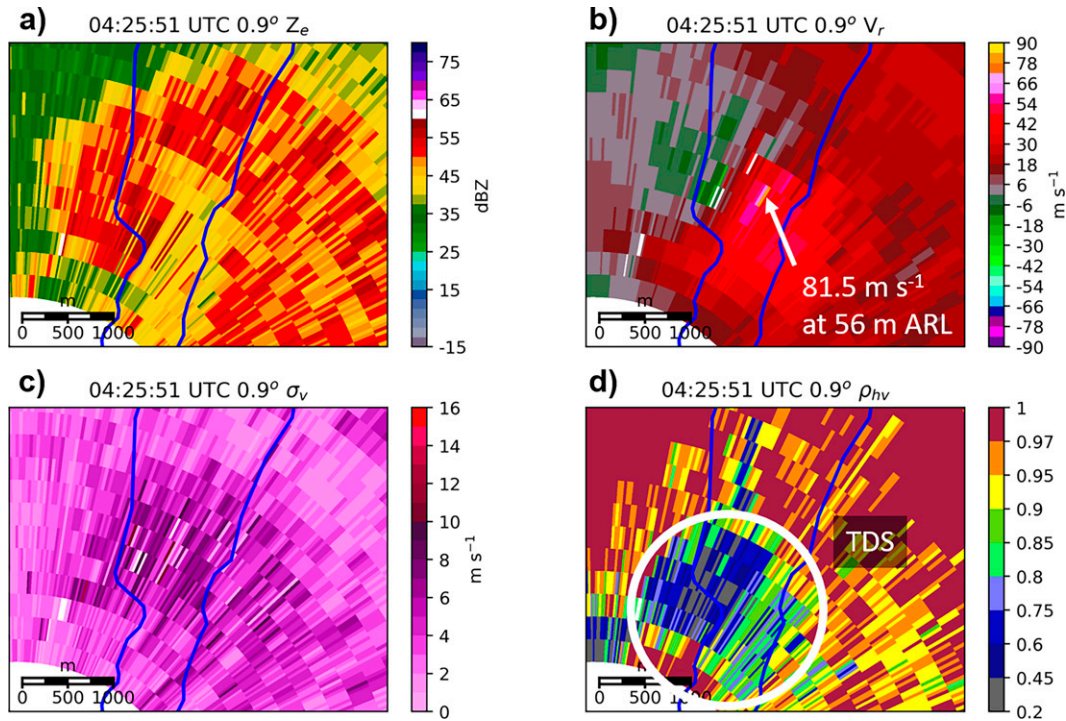
FIG. 11. Plan-position indicator (PPI) plots of (a) equivalent reflectivity factor (Z_e), (b) manually de-aliased radial velocity (V_r), (c) spectrum width (σ_v), and (d) copolar correlation coefficient (ρ_{hv}) from the 0.9° GWX sweep at 0425:51 UTC 14 Apr 2019, the time of the highest V_r value observed during the Greenwood Springs tornado. The EF0 damage contour of the tornado track is outlined in blue.

Russell, Kansas, tornado indicated a mean and median 10% decrease in wind speed between 10 and 40 m AGL (Kosiba and Wurman 2013). Similarly, observations from the Goshen County, Wyoming, tornado of 5 June 2009 indicate that the intensity of the tornado vortex likely peaked well below 50 m AGL (Wurman et al. 2013; French et al. 2014). While these research radar observations represent extremely small samples, they are consistent with large-eddy simulations (LES) performed by Lewellen et al. (1997), which indicated the likelihood of tornado winds reaching a peak intensity within 50 m of the surface. Both the available observations and simulations suggest an important sensitivity of tornado wind speeds to proximity to the ground. Given that GWX is located on a local area of higher elevation, that the total height of the land and tower exceeds any land around the region of inferred maximum intensity of the Greenwood Springs tornado, and the lowest elevation of any of the gates plotted in Fig. 10 is 47 m ARL, it seems unlikely that GWX would have sampled the maximum wind speed associated with the tornado, even if it had been sampling the vortex at its absolute peak intensity.

Not only is it evident that GWX observations do not necessarily represent the wind at 10 m AGL, but they also do not represent a 3-s gust. Analysis of individual sweep files in SOLO3 and Tables 5–6 in the Federal Meteorological Handbook No. 11 (OFCM 2017) provide a rotation rate between ~15° and 30° s^{-1} for GWX. Given that each radial for the super-resolution sweeps has an azimuthal sampling interval of

0.5°, data for each gate represents an approximate data collection time between 3.3×10^{-2} and 6.6×10^{-2} s. While these observations are collected over almost a full order of magnitude longer of a period than data from a rapid-scan radar (Snyder and Bluestein 2014), they still represent a far shorter gust time than the 3-s gust standard of the EF scale.

Although the integration period for each gate of data may be much shorter than the EF scale gust standard, the sample volume of a bin of WSR-88D datum is much larger than most mobile research radars. For example, the maximum Doppler velocity observed by GWX in the Greenwood Springs tornado of 81.5 m s^{-1} was observed at a mean range of 3.625 km from the radar. With a 250-m resolution volume range depth, the distance of the gate from the radar was approximately 3.5 to 3.75 km. While super resolution decreases the azimuthal sampling from 1.0° to 0.5°, the beamwidth remains 0.9°. Thus, given the observed 3.625-km range, 250-m resolution volume range depth, and a 0.9° beamwidth and assuming the volume of a column over the small distance of a radar range gate, the 81.5 m s^{-1} pixel represents a volume of 6.4×10^5 m^3. By comparison, the RSDOW utilized in Kosiba and Wurman (2013) has a 0.9° beamwidth (that oversamples at 0.3°–0.4°) and a resolution volume range depth of 25 m. A gate centered at a range of 3.625 km with a beamwidth of 0.9° and resolution volume range depth of 25 m would have a volume of 6.4×10^4 m^3. Given that the integration time for GWX is longer than rapid-scan radars and the bin volume is larger, it seems
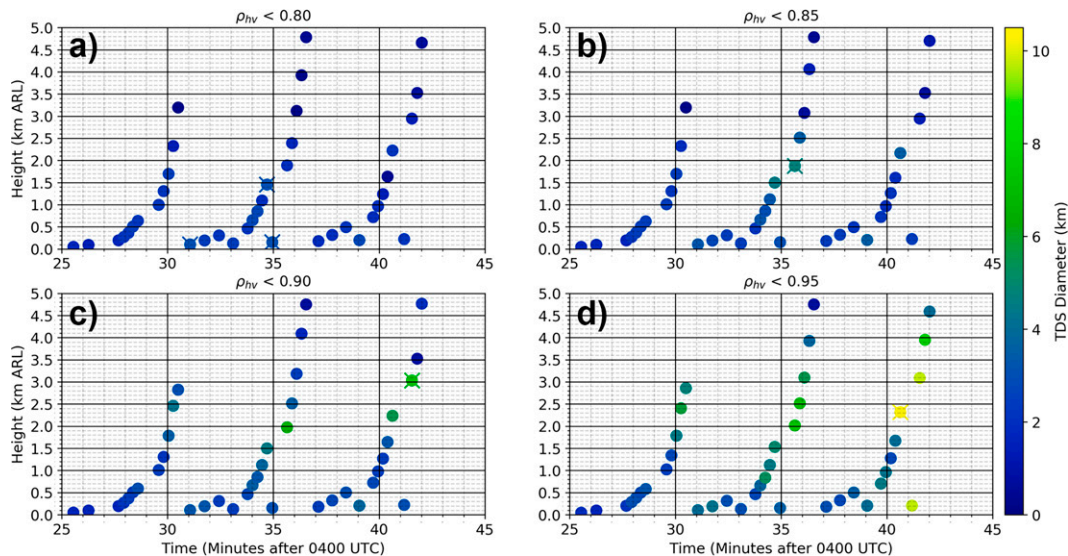
FIG. 12. Time–height scatterplots of TDS radial diameter at thresholds of (a) $\rho_{hv} < 0.80$, (b) $\rho_{hv} < 0.85$, (c) $\rho_{hv} < 0.90$, and (d) $\rho_{hv} < 0.95$ for the Greenwood Springs tornado from the GWX radar. Each point represents the midpoint between the lowest and highest mean pixel heights for pixels reaching each TDS threshold per scan. The time and mean height for the maximum diameter of the TDS for each threshold are denoted by the $\times$ symbol for reference.

likely that overestimates of the peak 3-s gust at 10 m AGL are lesser with the observations of the Greenwood Springs tornado than mobile radar observations of other tornadoes.

The frequency of observations from GWX during the life cycle of the Greenwood Springs tornado also serves to limit the ability to directly compare the radar observations with the damage caused by the tornado. The $15°–30° \text{ s}^{-1}$ antenna rotation rate on the lower elevation sweeps of GWX pale in comparison to the rotation rates of rapid-scanning radars, such as the $180° \text{ s}^{-1}$ rate on the University of Oklahoma Rapid-Scanning X-band Polarimetric (RaXPol) radar (Pazmany et al. 2013). The combination of the fast translation of the Greenwood Springs tornado and the slow data collection from GWX limited the total number of sweeps below 100 m ARL to five. While any low-level radar data collected in a forested area are exceedingly rare, the lack of continuous, high-resolution near-surface observations limits the comparison of radar data to the damage survey in this case to a primarily qualitative analysis.

The underlying land cover, coupled with the aforementioned terrain, further increases uncertainty in interpreting the radar observations from GWX. The mature wooded regions along the tornado track consisted of trees exceeding 20-m height. However, due to substantial tree farming in the area, these wooded regions were discontinuous, with much of the path consisting of a mixture of mature woods, densely packed but small, young, newly planted trees, and barren land, all sitting atop small wavelength, rough topography. A chaotic land surface such as that underlying the Greenwood Springs tornado may feature an aerodynamic roughness length (z_o) exceeding 1 m (Davenport 1960; Wieringa 1980). By comparison, Wurman et al. (2013) estimated the z_o values in the path of the Goshen County tornado to range between

0.01 and 0.04 m, and the LES experiments by Lewellen et al. (1997) utilized a z_o value of 0.2 m. While friction is thought to play a key role in tornado intensity being maximized near the surface through frictionally induced convergence of angular momentum (Lewellen et al. 1997), it is unclear how such significant values of z_o might impact the vertical profile of wind speed within a tornado.

Further complicating matters in attempting to characterize the low-level tornado structure, the violent tornado quickly lofted a tremendous quantity of tree debris into the vortex, as evidenced by the prominent 66.5-dBZ debris signature in Z_h in Fig. 14a. Dowell et al. (2005) illustrated the influence that debris loading can have on the Doppler velocity pattern associated with tornadoes, with debris loading leading to a broadening of the velocity couplet, weakening of the peak Doppler velocity magnitudes in the couplet, and radial displacement owing to centrifuging. Vertical profiles of V_{max} in the Greenwood Springs tornado indicate similar possible effects of debris on the velocity signature (Fig. 15). Early in the tornado life cycle (0424:49 UTC volume), V_{max} observed by GWX increased sharply with decreasing distance above the ground, similar to profiles of the Russell, Kansas, tornado of 25 May 2012 in Kosiba and Wurman (2013, their Fig. 4) and the El Reno, Oklahoma, tornado of 31 May 2013 in Snyder and Bluestein (2014, their Fig. 7). As evidenced by Fig. 11, which represents the 0.9° scan from this volume, debris was already being lofted (Fig. 11b), but the Z_h maximum was not as prominent as in Fig. 14a (Fig. 10a). By the 0431:04 UTC volume, the change of V_{max} with height below 2 km ARL was less, which may have been attributable to debris loading in the vortex.

Additional evidence of the influence of debris loading in the GWX velocity data can be found in Fig. 16. Early in the tornado's life cycle, the damage path and <200 m ARL
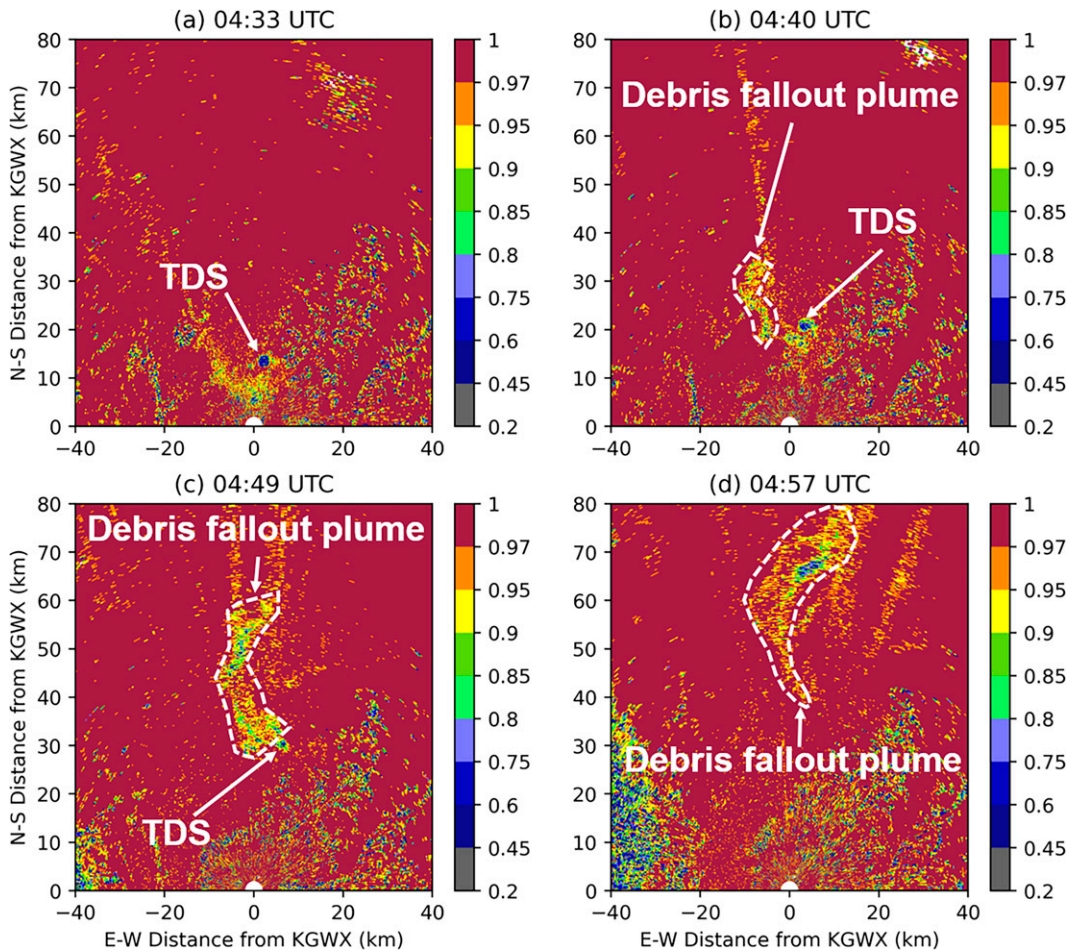
FIG. 13. 0.5° PPI plots of ρ_{hv} at (a) 0433, (b) 0440, (c) 0449, and (d) 0457 UTC 14 Apr 2019, illustrating the evolution of debris fallout associated with the Greenwood Springs tornado.

TDS diameter were each wider than the couplet diameter (Figs. 16a,c). As debris loading increased, the couplet diameter, as defined by the distance between the maximum inbound and outbound radial velocity values, surpassed the damage path width and approached the diameter of the TDS. Furthermore, as debris centrifuging from the vortex increased, the difference between the TDS diameter and damage path width increased (Fig. 16b). The broadening of the couplet as the tornado became loaded with debris leads to an obvious challenge when interpreting the relationship between the radar observations and damage. For example, low-level radar pixels directly over the house in Fig. 5 featured of V_r values in the EF3 wind gust range, with pixels in the EF4 range just east of the house (Fig. 17). However, the house did not sustain EF3–EF4 structural damage, and the most severe tree damage was located west of the house (Fig. 18). This rightward displacement of the maximum outbound V_r values associated with the tornadic circulation from the most intense portion of the damage path remained a consistent signal as the tornado continued northward and began to slowly weaken (Fig. 19). Such rightward displacement of the most intense V_r relative to the most

intense damage was also noted in the Spencer, South Dakota, tornado of 30 May 1998 (Dowell et al. 2005; Wurman and Alexander 2005). The center of the couplet also became displaced to the west of the track as tornado moved past the region of most intense damage and began to weaken (left of the forward motion; Fig. 16e). This westward displacement is likely attributable to the combination of the circulation weakening and the "canceling" effect of the fast forward motion on the tangential velocity component opposing the forward motion of the tornado. Given the combination of the sharp drop in V_{ROT} and weaker damage after 0429 UTC (Fig. 16d), it is possible that some of the weakening of the tornado itself after it produced EF4 damage was directly due to the debris loading (e.g., Lewellen et al. 2008), but separating those effects from other tornado-scale and storm-scale processes, such as the influence of the RFD microburst detailed in Fig. 14 on the tornado structure, is impossible with this dataset.

While debris loading of the funnel complicated the relationship between the GWX observations and the damage, the survival of the house in Fig. 5 still raises questions about how to evaluate tornado intensity in forested areas, given the significant tree damage surrounding it. It seems plausible that the
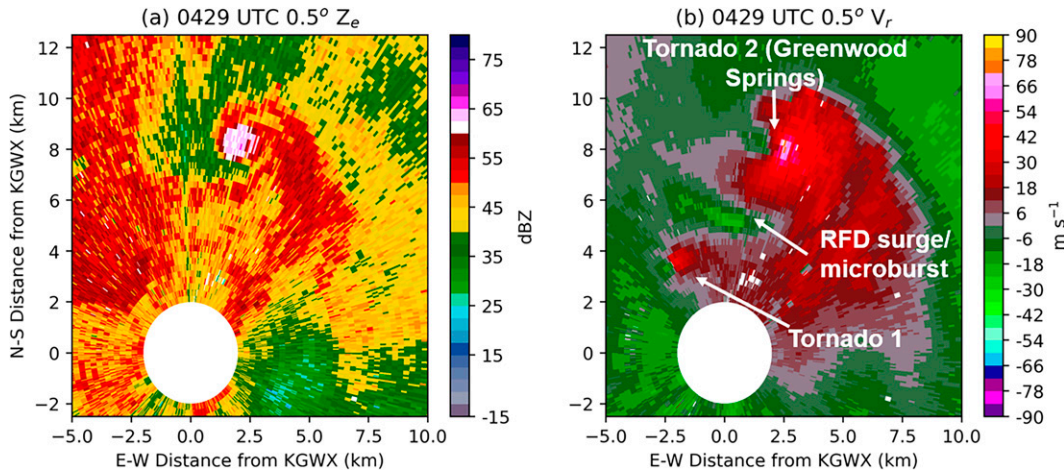
FIG. 14. (a) 0.5° PPIs of Z_e and (b) V_r at 0429 UTC 14 Apr 2019, showing the location of the rear-flank microburst relative to the Greenwood Springs tornado ("Tornado 2"), as well as the initial tornado associated with the parent supercell ("Tornado 1").

trees may have sheltered the structure from the strongest winds of the tornado, allowing the structure to remain standing even as most trees were snapped, uprooted, or stripped around it. Most of these mature trees were much greater than 10 m tall, while the one-story house was less than ~5 m tall. Tree-fall fraction was at least 75% surrounding the house, which would suggest EF2–EF3 damage intensity on the Canadian EF scale, but the house itself suffered minimal damage other than that caused by trees falling on it. The question remains that if the trees are modifying the vertical wind profile of the tornado such that the wind speeds causing the tree damage are much greater than the actual 10-m wind speed in these forested areas, then which wind speed should be used to evaluate the intensity of the tornado?
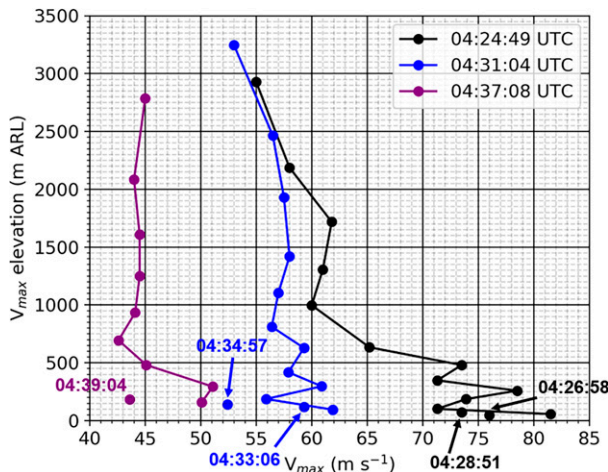

FIG. 15. Vertical profiles of maximum outbound radial velocity (V_{max}) of the couplet associated with the Greenwood Springs tornado from the GWX radar for the 0424:49, 0431:04, and 0437:08 UTC 14 Apr 2019 volume times. Values annotated with times but not on the profile lines are from the extra MESO-SAILS 0.5°sweeps from each volume.

6. Summary and conclusions

Ground survey information, aerial photography, and close-range observations from the GWX WSR-88D all illustrate that the Greenwood Springs tornado was large and violent. Damage indicators along the track supported a maximum rating of at least EF4 on the EF scale, with the most intense damage consisting of near-100% blowdown of large swaths of mature woodland in the core of the damage path at peak intensity The peak radial velocity sampled by the GWX WSR-88D radar was 81.5 m s^{-1} at an elevation of 56 m ARL. The TDS associated with the tornado was immediately large as the tornado moved out of the "no data" region of the GWX radar and displayed a classical evolution of debris loading and dispersion as the tornado slowly weakened and eventually dissipated.

This study highlights some of the challenges in relating tornado intensity to radar observations and in assessing tornado damage intensity, particularly once substantial debris has been lofted into the vortex. While close-range observations from the GWX radar exist, comparison of the radar observations to tree damage is complicated by the fact that the radar-inferred vertical wind profile of the tornado differed substantially from the observed peak-intensity damage, despite some of the radar observations being collected at an estimated mean beam height below 50 m ARL. Nonetheless, the extreme tree damage observed along the track near the strongest V_r observations from GWX lends credence to the findings from Godfrey and Peterson (2017) and the Canadian EF scale that extreme tree-fall fraction (>95% over a 100 m × 100 m area) may most likely be associated with violent (EF4–EF5) tornadic winds. Qualitative comparison to the results from the Rankine vortex model estimation of tornado intensity based on tree-fall pattern from H06 also suggested that the Greenwood Springs event was a violent tornado, potentially even EF5 intensity.
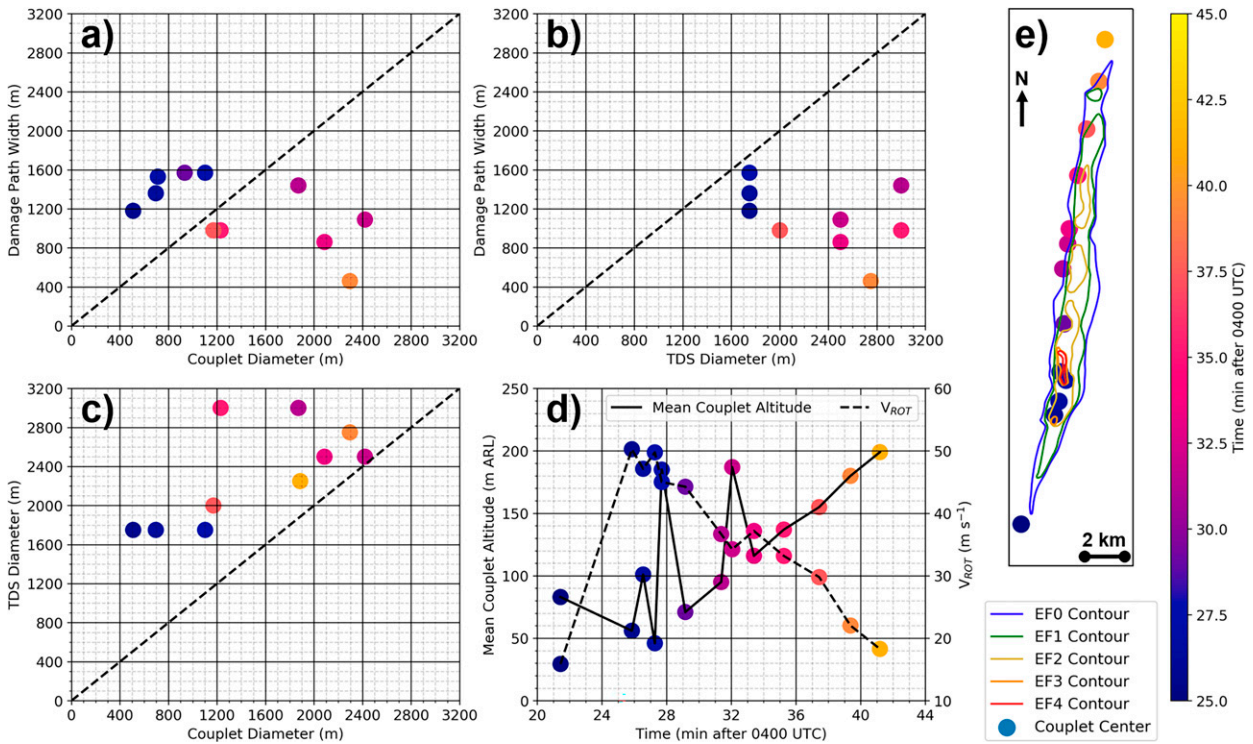
FIG. 16. Scatterplots of (a) damage path width as a function of couplet diameter, (b) damage path width as a function of TDS diameter, and (c) TDS diameter as a function of couplet diameter for all GWX observations where the couplet from GWX was centered at or below 200 m ARL. (d) Time series of mean couplet altitude and V_{ROT} and (e) a map overlaying couplet center points with the EF contours of the tornado track are supplied for reference.

Additionally, this study showcases the fundamental weakness of the current operational EF scale DIs for trees in the United States. Not only do the near-surface velocity observations from the GWX radar support the Greenwood Springs

tornado being violent, despite extensive debris loading of the vortex, but the metrics of the TDS extent, particularly depth, exceed the mean values observed in intense ($\geq$EF3) tornadoes. Tornado intensity estimation and climatology
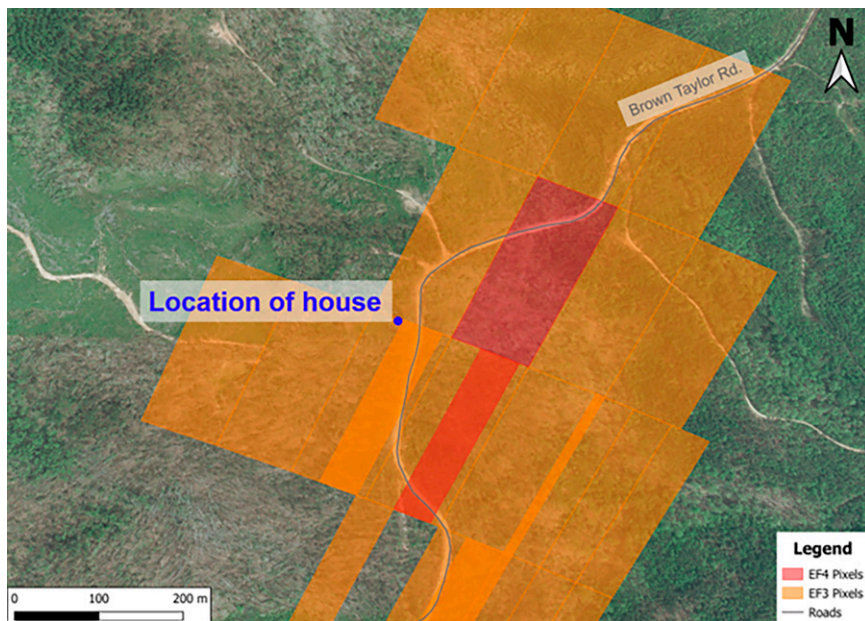

FIG. 17. Zoomed-in map of the pixels with V_r values in the EF3+ range overlaid with aerial imagery and the location of the house pictured in Fig. 5 along Brown Taylor Road.
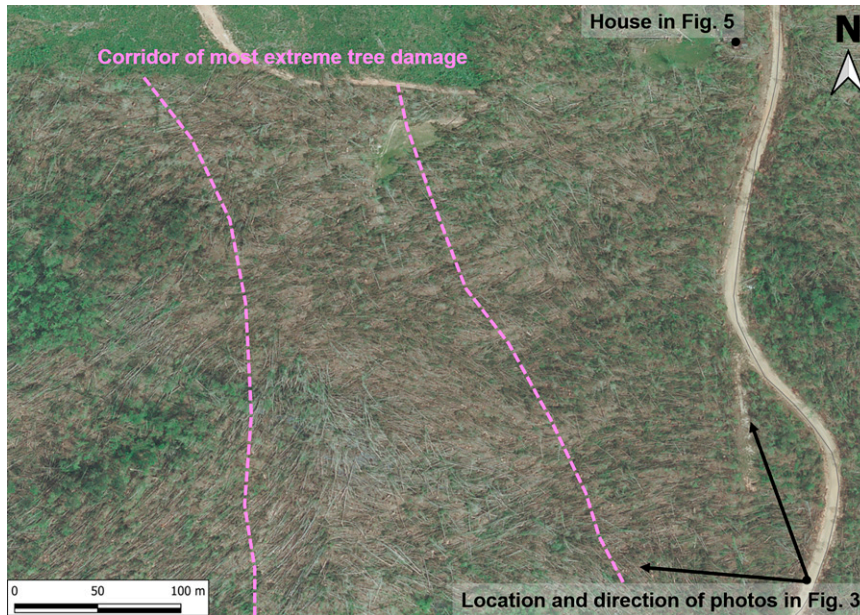
FIG. 18. Aerial imagery of the beginning of the most intense tree damage swath (rated EF4) associated with the Greenwood Springs tornado and the positions of the images shown in Figs. 3 and 5 overlaid.

contain numerous systematic flaws (Edwards et al. 2013), and past studies comparing close-range radar, near-surface (<200 m ARL) observations to damage analysis have found inconsistencies between radar-measured Doppler velocity and damage-derived intensity estimates (e.g., Wurman and Alexander 2005; Wurman et al. 2013; Wakimoto et al.

2016). However, the estimation of tornado intensity from tree-fall fraction yielded a result that is far better aligned with the GWX radar observations and is likely far more representative of the actual intensity of the tornado.

Furthermore, the survival of a house near the maximum damage intensity raises questions about how similar the
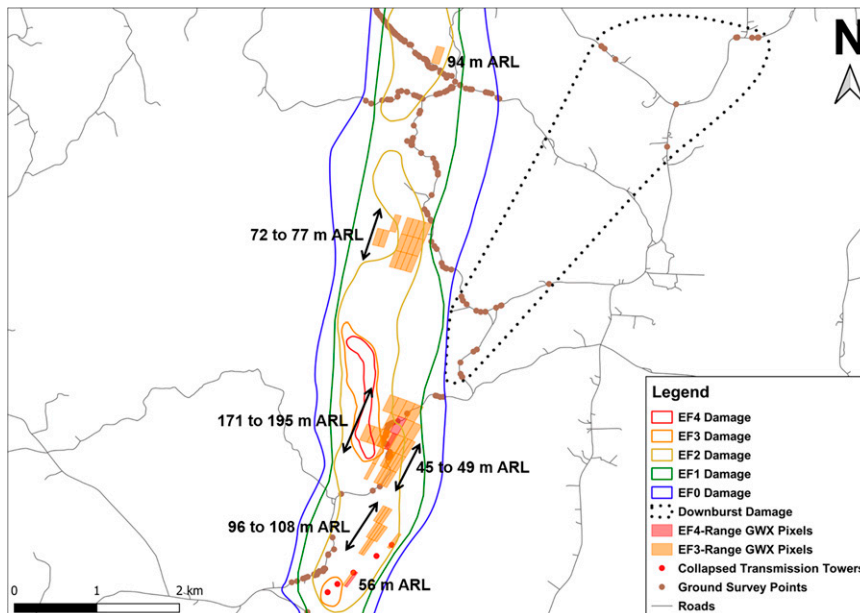

FIG. 19. Zoomed-in map of the most intense damage region of the Greenwood Springs tornado with GWX pixels featuring V_r values in the EF3 or EF4 wind speed range overlaid. The elevation values indicate the range of estimated beam heights for pixels in each GWX sweep where EF3+ V_r values are detected.

near-surface wind profile of a tornado moving over a higher-roughness surface is to the observations of near-surface tornado wind profiles collected over the relatively smooth, open Great Plains region. Given that the EF scale standard is an estimated 3-s gust speed at 10 m AGL, should such an estimate be adjusted for damage in densely forested areas, where shelter effects from the tree canopy may otherwise lessen the 10-m wind speed? How does the tornado wind speed profile respond as a large percentage of underlying timber falls? These questions remain unresolved in this study. However, this study does emphasize the need to use extensive caution when interpreting the wind speeds measured in tornadoes by Doppler radar and inferring the intensity of a tornado from them, even when those observations are at close-range and close to the ground. The representativeness of radar observations relative to the 3-s gust standard of the EF scale is unclear, as is how the vertical wind profile of a tornado near the surface may differ across differing terrain, land cover, land use, and surface roughness, as well as in different environments.

To the authors' knowledge, the Greenwood Springs tornado study presented herein is unprecedented in formal literature in its presentation of near-surface (<100 m ARL) radar observations in a region of dense tree cover. While similar studies of any future serendipitous cases are certainly encouraged, further advancement of understanding many of the questions posed by this dataset will be more feasible through controlled simulation experiments. Large-eddy simulations akin to those used to study tornado structure (e.g., Lewellen et al. 1997) and the impacts of debris loading (Lewellen et al. 2008; Bodine et al. 2016) and underlying terrain (Satrio et al. 2020) could prove useful in understanding the interplay between tornadoes and the surface in regions of dense tree cover.

Data availability statement. WSR-88D data are available publicly for download via NCEI (https://www.ncdc.noaa.gov/nexradinv/). Pictures from the author-lead ground damage survey can be accessed here: https://www.dropbox.com/sh/ 1kmy2nt45tyyzhq/AADjFNFb1pYLUKIxL5NbgnU-a?dl=0, and ground damage images from NWS MEG's survey can be accessed through the damage assessment toolkit (https:// apps.dat.noaa.gov/stormdamage/damageviewer/). Aerial photography can be obtained upon request. The digital elevation model used in Fig. 6 can be accessed from the U.S. Geological Survey (https://www.sciencebase.gov/catalog/ item/5eacf03482cefae35a24c279).

REFERENCES

Agee, E., and S. Childs, 2014: Adjustments in tornado counts, F-scale intensity, and path width for assessing significant tornado destruction. *J. Appl. Meteor. Climatol.*, **53**, 1494–1505, https://doi.org/10.1175/JAMC-D-13-0235.1.

Alexander, C., and J. Wurman, 2005: The 30 May 1998 Spencer, South Dakota, storm. Part I: The structural evolution and environment of the tornadoes. *Mon. Wea. Rev.*, **133**, 72–97, https://doi.org/10.1175/MWR-2855.1.

Ashley, W. S., 2007: Spatial and temporal analysis of tornado fatalities in the United States: 1880–2005. *Wea. Forecasting*, **22**, 1214–1228, https://doi.org/10.1175/2007WAF2007004.1.

——, A. J. Krmenec, and R. Schwantes, 2008: Vulnerability due to nocturnal tornadoes. *Wea. Forecasting*, **23**, 795–807, https:// doi.org/10.1175/2008WAF2222132.1.

Atkins, N. T., A. McGee, R. Ducharme, R. M. Wakimoto, and J. Wurman, 2012: The LaGrange tornado during VORTEX2. Part II: Photogrammetric analysis of the tornado combined with dual-Doppler radar data. *Mon. Wea. Rev.*, **140**, 2939–2958, https://doi.org/10.1175/MWR-D-11-00285.1.

Beck, V., and N. Dotzek, 2010: Reconstruction of near-surface tornado wind fields from forest damage. *J. Appl. Meteor. Climatol.*, **49**, 1517–1537, https://doi.org/10.1175/2010JAMC2254.1.

Blair, S. F., D. R. Deroche, and A. E. Pietrycha, 2008: In situ observations of the 21 April 2007 Tulia, Texas tornado. *Electron. J. Severe Storms Meteor.*, **3** (3), https://ejssm.org/archives/wp-content/uploads/2021/09/vol3-3.pdf.

Blanchard, D. O., 2013: A comparison of wind speed and forest damage associated with tornadoes in northern Arizona. *Wea. Forecasting*, **28**, 408–417, https://doi.org/10.1175/WAF-D-12-00046.1.

Bluestein, H. B., and A. L. Pazmany, 2000: Observations of tornadoes and other convective phenomena with a mobile, 3-mm wavelength, Doppler radar: The spring 1999 field experiment. *Bull. Amer. Meteor. Soc.*, **81**, 2939–2951, https://doi.org/10.1175/1520-0477(2000)081<2939:OOTAOC>2.3.CO;2.

——, W.-C. Lee, M. Bell, C. C. Weiss, and A. L. Pazmany, 2003a: Mobile Doppler radar observations of a tornado in a supercell near Bassett, Nebraska, on 5 June 1999. Part II: Tornado-vortex structure. *Mon. Wea. Rev.*, **131**, 2968–2984, https://doi.org/10.1175/1520-0493(2003)131<2968:MDROOA>2.0.CO;2.

——, C. C. Weiss, and A. L. Pazmany, 2003b: Mobile Doppler radar observations of a tornado in a supercell near Bassett, Nebraska, on 5 June 1999. Part I: Tornadogenesis. *Mon. Wea. Rev.*, **131**, 2954–2967, https://doi.org/10.1175/1520-0493(2003)131<2954:MDROOA>2.0.CO;2.

——, ——, and ——, 2004: The vertical structure of a tornado near Happy, Texas, on 5 May 2002: High-resolution, mobile, W-band, Doppler radar observations. *Mon. Wea. Rev.*, **132**, 2325–2337, https://doi.org/10.1175/1520-0493(2004)132<2325:TVSOAT>2.0.CO;2.

——, M. M. French, R. L. Tanamachi, S. Frasier, K. Hardwick, F. Junyent, and A. L. Pazmany, 2007a: Close-range observations of tornadoes in supercells made with a dual-polarization, X-band, mobile Doppler radar. *Mon. Wea. Rev.*, **135**, 1522–1543, https://doi.org/10.1175/MWR3349.1.

——, C. C. Weiss, M. M. French, E. M. Holthaus, R. L. Tanamachi, S. Frasier, and A. L. Pazmany, 2007b: The structure of tornadoes near Attica, Kansas, on 12 May 2004: High-resolution, mobile, Doppler radar observations. *Mon. Wea. Rev.*, **135**, 475–506, https://doi.org/10.1175/MWR3295.1.

——, J. C. Synder, and J. B. Houser, 2015: A multiscale overview of the El Reno, Oklahoma, tornadic supercell of 31 May 2013. *Wea. Forecasting*, **30**, 525–552, https://doi.org/10.1175/WAF-D-14-00152.1.

——, M. M. French, J. C. Snyder, and J. B. Houser, 2016: Doppler radar observations of anticyclonic tornadoes in cyclonically rotating, right-moving supercells. *Mon. Wea. Rev.*, **144**, 1591–1616, https://doi.org/10.1175/MWR-D-15-0304.1.

——, K. J. Thiem, J. C. Snyder, and J. B. Houser, 2018: The multiple-vortex structure of the El Reno, Oklahoma, tornado on 31 May 2013. *Mon. Wea. Rev.*, **146**, 2483–2502, https://doi.org/10.1175/MWR-D-18-0073.1.

——, ——, ——, and ——, 2019: Tornadogenesis and early tornado evolution in the El Reno, Oklahoma, supercell on 31 May 2013. *Mon. Wea. Rev.*, **147**, 2045–2066, https://doi.org/10.1175/MWR-D-18-0338.1.

Bodine, D. J., M. R. Kumjian, R. D. Palmer, P. L. Heinselman, and A. V. Ryzhkov, 2013: Tornado damage estimation using polarimetric radar. *Wea. Forecasting*, **28**, 139–158, https://doi.org/10.1175/WAF-D-11-00158.1.

——, T. Maruyama, R. D. Palmer, C. J. Fulton, H. B. Bluestein, and D. C. Lewellen, 2016: Sensitivity of tornado dynamics to soil debris loading. *J. Atmos. Sci.*, **73**, 2783–2801, https://doi.org/10.1175/JAS-D-15-0188.1.

Brooks, H. E., C. A. Doswell III, and M. P. Kay, 2003: Climatological estimates of local daily tornado probability for the United States. *Wea. Forecasting*, **18**, 626–640, https://doi.org/10.1175/1520-0434(2003)018<0626:CEOLDT>2.0.CO;2.

Brown, R. A., B. A. Flickinger, E. Forren, D. M. Schultz, D. Sirmans, P. L. Spencer, V. T. Wood, and C. L. Ziegler, 2005: Improved detection of severe storms using experimental fine-resolution WSR-88D measurements. *Wea. Forecasting*, **20**, 3–14, https://doi.org/10.1175/WAF-832.1.

Burgess, D. W., M. A. Magsig, J. Wurman, D. C. Dowell, and Y. Richardson, 2002: Radar observations of the 3 May 1999 Oklahoma City tornado. *Wea. Forecasting*, **17**, 456–471, https://doi.org/10.1175/1520-0434(2002)017<0456:ROOTMO>2.0.CO;2.

Chrisman, J., 2014: Multiple Elevation Scan Option for SAILS (MESO-SAILS). NWS/Radar Operations Center, 27 pp., https://www.roc.noaa.gov/WSR88D/PublicDocs/NewTechnology/MESO-SAILS_Description_Briefing_Jan_2014.pdf.

Coleman, T. A., and P. G. Dixon, 2014: An objective analysis of tornado risk in the United States. *Wea. Forecasting*, **29**, 366–376, https://doi.org/10.1175/WAF-D-13-00057.1.

Davenport, A. G., 1960: Rationale for determining design wind velocities. *J. Struct. Div., Amer. Soc. Civ. Eng.*, **86**, 39–68, https://doi.org/10.1061/JSDEAG.0000521.

Dixon, P. G., A. E. Mercer, J. Choi, and J. S. Allen, 2011: Tornado risk analysis: Is Dixie Alley an extension of Tornado Alley? *Bull. Amer. Meteor. Soc.*, **92**, 433–441, https://doi.org/10.1175/2010BAMS3102.1.

Dowell, D. C., C. R. Alexander, J. M. Wurman, and L. J. Wicker, 2005: Centrifuging of hydrometeors and debris in tornadoes: Radar-reflectivity patterns and wind-measurement errors. *Mon. Wea. Rev.*, **133**, 1501–1524, https://doi.org/10.1175/MWR2934.1.

Dunn, L. B., and S. V. Vasiloff, 2001: Tornadogenesis and operational considerations of the 11 August 1999 Salt Lake City tornado as seen from two different Doppler radars. *Wea. Forecasting*, **16**, 377–398, https://doi.org/10.1175/1520-0434(2001)016<0377:TAOCOT>2.0.CO;2.

Edwards, R., J. G. LaDue, J. T. Ferree, K. Scharfenberg, C. Maier, and W. L. Coulbourne, 2013: Tornado intensity estimation: Past, present, and future. *Bull. Amer. Meteor. Soc.*, **94**, 641–653, https://doi.org/10.1175/BAMS-D-11-00006.1.

Environment Canada, 2021: Enhanced Fujita scale damage indicators and degrees of damage, chapter 27: C-2 Trees (C-T). Accessed 15 December 2021, https://www.canada.ca/en/environment-climate-change/services/seasonal-weather-hazards/publications/enhanced-fujita-scale-damage-indicators/chapter-27.html.

Feuerstein, B., N. Dotzek, and J. Grieser, 2005: Assessing a tornado climatology from global tornado intensity distributions. *J. Climate*, **18**, 585–596, https://doi.org/10.1175/JCLI-3285.1.

Forbes, G. S., 1998: Topographic influences on tornadoes in Pennsylvania. Preprints, *19th Conf. on Severe Local Storms*, Minneapolis, MN, Amer. Meteor. Soc., 269–272.

French, M. M., H. B. Bluestein, I. PopStefanija, C. A. Baldi, and R. T. Bluth, 2013: Reexamining the vertical development of tornadic vortex signatures in supercells. *Mon. Wea. Rev.*, **141**, 4576–4601, https://doi.org/10.1175/MWR-D-12-00315.1.

——, ——, ——, ——, and ——, 2014: Mobile, phased-array, Doppler radar observations of tornadoes at X band. *Mon. Wea. Rev.*, **142**, 1010–1036, https://doi.org/10.1175/MWR-D-13-00101.1.

——, ——, L. J. Wicker, D. C. Dowell, and M. R. Kramar, 2009: An example of the use of mobile, Doppler radar data for tornado verification. *Wea. Forecasting*, **24**, 884–891, https://doi.org/10.1175/2008WAF2222147.1.

——, P. S. Skinner, L. J. Wicker, and H. B. Bluestein, 2015: Documenting a rare tornado merger observed in the 24 May 2011 El Reno–Piedmont, Oklahoma, supercell. *Mon. Wea. Rev.*, **143**, 3025–3043, https://doi.org/10.1175/MWR-D-14-00349.1.

Fuhrmann, C. M., C. E. Konrad II, M. M. Kovach, J. T. McLeod, W. G. Schmitz, and P. G. Dixon, 2014: Ranking of tornado outbreaks across the United States and their climatological characteristics. *Wea. Forecasting*, **29**, 684–701, https://doi.org/10.1175/WAF-D-13-00128.1.

Fujita, T. T., 1989: The Teton–Yellowstone tornado of 21 July 1989. *Mon. Wea. Rev.*, **117**, 1913–1940, https://doi.org/10.1175/1520-0493(1989)117<1913:TTYTOJ>2.0.CO;2.

Gibbs, J. G., 2016: A skill assessment of techniques for real-time diagnosis and short-term prediction of tornado intensity using the WSR-88D. *J. Oper. Meteor.*, **4**, 170–181, https://doi.org/10.15191/nwajom.2016.0413.

——, and B. R. Bowers, 2019: Techniques and thresholds of significance for using WSR-88D velocity data to anticipate significant tornadoes. *J. Oper. Meteor.*, **7**, 117–137, https://doi.org/10.15191/nwajom.2019.0709.

Godfrey, C. M., and C. J. Peterson, 2017: Estimating enhanced Fujita scale levels based on forest damage severity. *Wea. Forecasting*, **32**, 243–252, https://doi.org/10.1175/WAF-D-16-0104.1.

Griffin, C. B., D. J. Bodine, J. M. Kurdzo, A. Mahre, and R. D. Palmer, 2019: High-temporal resolution observations of the 27 May 2015 Canadian, Texas, tornado using the Atmospheric Imaging Radar. *Mon. Wea. Rev.*, **147**, 873–891, https://doi.org/10.1175/MWR-D-18-0297.1.

Helmus, J. J., and S. M. Collis, 2016: The Python ARM Radar Toolkit (Py-ART), a library for working with weather radar data in the Python programming language. *J. Open Res. Software*, **4**, e25, https://doi.org/10.5334/jors.119.

Holland, A. P., A. J. Riordan, and E. C. Franklin, 2006: A simple model for simulating tornado damage in forests. *J. Appl. Meteor. Climatol.*, **45**, 1597–1611, https://doi.org/10.1175/JAM2413.1.

Houser, J. L., H. B. Bluestein, and J. C. Snyder, 2015: Rapid-scan, polarimetric, Doppler radar observations of tornadogenesis and tornado dissipation in a tornadic supercell: The "El Reno, Oklahoma" storm of 24 May 2011. *Mon. Wea. Rev.*, **143**, 2685–2710, https://doi.org/10.1175/MWR-D-14-00253.1.

——, ——, and ——, 2016: A finescale radar examination of the tornadic debris signature and weak-echo reflectivity band associated with a large, violent tornado. *Mon. Wea. Rev.*, **144**, 4101–4130, https://doi.org/10.1175/MWR-D-15-0408.1.

Houser, J. B., N. McGinnis, K. M. Butler, H. B. Bluestein, J. C. Snyder, and M. M. French, 2020: Statistical and empirical relationships between tornado intensity and both topography and land cover using rapid-scan radar observations and a GIS. *Mon. Wea. Rev.*, **148**, 4313–4338, https://doi.org/10.1175/MWR-D-19-0407.1.

IEM, 2020: National Weather Service Raw Text Product. Iowa State University, Iowa Environmental Mesonet, accessed 5 May 2020, https://mesonet.agron.iastate.edu/wx/afos/p.php?pil=PNSMEG&e=201904151837.

Jedlovec, G. J., U. Nair, and S. L. Haines, 2006: Detection of storm damage tracks with EOS data. *Wea. Forecasting*, **21**, 249–267, https://doi.org/10.1175/WAF923.1.

Karstens, C. D., T. M. Samaras, B. D. Lee, W. A. Gallus Jr., and C. A. Finley, 2010: Near-ground pressure and wind measurements in tornadoes. *Mon. Wea. Rev.*, **138**, 2570–2588, https://doi.org/10.1175/2010MWR3201.1.

——, W. A. Gallus Jr., B. D. Lee, and C. A. Finley, 2013: Analysis of tornado-induced tree fall using aerial photography from the Joplin, Missouri, and Tuscaloosa–Birmingham, Alabama, tornadoes of 2011. *J. Appl. Meteor. Climatol.*, **52**, 1049–1068, https://doi.org/10.1175/JAMC-D-12-0206.1.

Kingfield, D. M., and J. G. LaDue, 2015: The relationship between automated low-level velocity calculations from the WSR-88D and maximum tornado intensity determined from damage surveys. *Wea. Forecasting*, **30**, 1125–1139, https://doi.org/10.1175/WAF-D-14-00096.1.

——, and K. M. de Beurs, 2017: Landsat identification of tornado damage by land cover and an evaluation of damage recovery in forests. *J. Appl. Meteor. Climatol.*, **56**, 965–987, https://doi.org/10.1175/JAMC-D-16-0228.1.

Kis, A. K., and J. M. Straka, 2010: Nocturnal tornado climatology. *Wea. Forecasting*, **25**, 545–561, https://doi.org/10.1175/2009WAF2222294.1.

Klees, A. M., Y. P. Richardson, P. M. Markowski, C. Weiss, J. M. Wurman, and K. A. Kosiba, 2016: Comparison of the tornadic and nontornadic supercells intercepted by VORTEX2 on 10 June 2010. *Mon. Wea. Rev.*, **144**, 3201–3231, https://doi.org/10.1175/MWR-D-15-0345.1.

Kosiba, K., and J. Wurman, 2013: The three-dimensional structure and evolution of a tornado boundary layer. *Wea. Forecasting*, **28**, 1552–1561, https://doi.org/10.1175/WAF-D-13-00070.1.

——, ——, Y. Richardson, P. Markowski, P. Robinson, and J. Marquis, 2013: Genesis of the Goshen County, Wyoming, tornado on 5 June 2009 during VORTEX2. *Mon. Wea. Rev.*, **141**, 1157–1181, https://doi.org/10.1175/MWR-D-12-00056.1.

Krocak, M. J., and H. E. Brooks, 2018: Climatological estimates of hourly tornado probability for the United States. *Wea. Forecasting*, **33**, 59–69, https://doi.org/10.1175/WAF-D-17-0123.1.

LaDue, J. G., 2016: About the ASCE Tornado Wind Speed Estimation Standards Committee. *28th Conf. on Severe Local Storms*, Portland, OR, Amer. Meteor. Soc., 6B.1, https://ams.confex.com/ams/28SLS/webprogram/Paper300684.html.

——, K. Ortega, B. Smith, G. Stumpf, and D. M. Kingfield, 2012: A comparison of high resolution tornado surveys to Doppler radar observed mesocyclone parameters: 2011–2012 case studies. *26th Conf. on Severe Local Storms*, Nashville, TN, Amer. Meteor. Soc., 6.3, https://ams.confex.com/ams/26SLS/webprogram/Paper212627.html.

——, J. Wurman, M. Levitan, F. T. Lombardo, C. D. Karstens, J. Robinson, and W. Coulbourne, 2018: Advances in development of the ASCE/SEI/AMS standard for wind speed estimation in tornadoes and other windstorms. *29th Conf. on Severe Local Storms*, Stowe, VT, Amer. Meteor. Soc., 29, https://ams.confex.com/ams/29SLS/webprogram/Paper348726.html.

Lee, B. D., C. A. Finley, and T. A. Samaras, 2011: Surface analysis near and within the Tipton, Kansas, tornado on 29 May 2008. *Mon. Wea. Rev.*, **139**, 370–386, https://doi.org/10.1175/2010MWR3454.1.

Lee, W.-C., and J. Wurman, 2005: Diagnosed three-dimensional axisymmetric structure of the Mulhall tornado on 3 May 1999. *J. Atmos. Sci.*, **62**, 2373–2393, https://doi.org/10.1175/JAS3489.1.

Lepore, C., and M. K. Tippett, 2020: Environmental controls on the climatological scaling of tornado frequency with intensity. *Mon. Wea. Rev.*, **148**, 4467–4478, https://doi.org/10.1175/MWR-D-20-0138.1.

Lewellen, D. C., B. Gong, and W. S. Lewellen, 2008: Effects of finescale debris on near-surface tornado dynamics. *J. Atmos. Sci.*, **65**, 3247–3262, https://doi.org/10.1175/2008JAS2686.1.

Lewellen, W. S., D. C. Lewellen, and R. I. Sykes, 1997: Large-eddy simulation of a tornado's interaction with the surface. *J. Atmos. Sci.*, **54**, 581–605, https://doi.org/10.1175/1520-0469(1997)054<0581:LESOAT>2.0.CO;2.

Lombardo, F. T., D. B. Roueche, and D. O. Prevatt, 2015: Comparison of two methods of near-surface wind speed estimation in the 22 May, 2011 Joplin, Missouri tornado. *J. Wind Eng. Ind. Aerodyn.*, **138**, 87–97, https://doi.org/10.1016/j.jweia.2014.12.007.

Lyza, A. W., R. Castro, E. Lenning, M. T. Friedlein, B. S. Borchardt, A. W. Clayton, and K. R. Knupp, 2019: A multiplatform reanalysis of the Kankakee Valley tornado cluster on 30 June 2014. *Electron. J. Severe Storms Meteor.*, **14** (3), https://ejssm.org/archives/2019/vol-14-3-2019/.

——, B. T. Goudeau, and K. R. Knupp, 2020a: Close-range radar observations and high-resolution damage survey of a large, intense tornado in a forested area during the VORTEX-SE Meso18-19 field campaign. *20th Symp. on Meteorological Observation and Instrumentation*, Boston, MA,

Amer. Meteor. Soc., 3.1, https://ams.confex.com/ams/2020Annual/meetingapp.cgi/Paper/369478.

——, T. A. Murphy, B. T. Goudeau, P. T. Pangle, K. R. Knupp, and R. A. Wade, 2020b: Observed near-storm environment variations across the southern Cumberland Plateau system in northeastern Alabama. *Mon. Wea. Rev.*, **148**, 1465–1482, https://doi.org/10.1175/MWR-D-19-0190.1.

Mahre, A., J. M. Kurdzo, D. J. Bodine, C. B. Griffin, R. D. Palmer, and T.-Y. Yu, 2018: Analysis of the 16 May 2015 Tipton, Oklahoma, EF-3 tornado at high spatiotemporal resolution using the Atmospheric Imaging Radar. *Mon. Wea. Rev.*, **146**, 2103–2124, https://doi.org/10.1175/MWR-D-17-0256.1.

Marquis, J., Y. Richardson, J. Wurman, and P. Markowski, 2008: Single- and dual-Doppler analysis of a tornadic vortex and surrounding storm-scale flow in the Crowell, Texas, supercell of 30 April 2000. *Mon. Wea. Rev.*, **136**, 5017–5043, https://doi.org/10.1175/2008MWR2442.1.

McKeown, K. E., M. M. French, K. S. Tuftedal, D. M. Kingfield, H. B. Bluestein, D. W. Reif, and Z. B. Wienhoff, 2020: Rapid-scan and polarimetric radar observations of the dissipation of a violent tornado on 9 May 2016 near Sulphur, Oklahoma. *Mon. Wea. Rev.*, **148**, 3951–3971, https://doi.org/10.1175/MWR-D-20-0033.1.

Molthan, A. L., J. R. Bell, T. A. Cole, and J. E. Burks, 2014: Satellite-based identification of tornado damage tracks from the 27 April 2011 severe weather outbreak. *J. Oper. Meteor.*, **2**, 191–208, https://doi.org/10.15191/nwajom.2014.0216.

NWS, 2021: JetStream Max: Volume Coverage Patterns (VCPs). Accessed 1 October 2021, https://www.weather.gov/jetstream/vcp_max.

OFCM, 2017: WSR-88D meteorological observations, Part C: WSR-88D products and algorithms. Federal Meteorological Handbook 11, Tech. Doc. FCM-H11C-2017, 396 pp., https://www.icams-portal.gov/resources/ofcm/fmh/FMH11/fmh11partC.pdf.

Oye, R., C. Mueller, and S. Smith, 1995: Software for radar translation, visualization, editing, and interpolation. Preprints, *27th Conf. on Radar Meteorology*, Vail, CO, Amer. Meteor. Soc., 359–361.

Pazmany, A. L., J. B. Mead, H. B. Bluestein, J. C. Snyder, and J. B. Houser, 2013: A mobile Rapid-Scanning X-band Polarimetric (RaXPol) Doppler radar system. *J. Atmos. Oceanic Technol.*, **30**, 1398–1413, https://doi.org/10.1175/JTECH-D-12-00166.1.

Rankine, W. J. M., 1901: *A Manual of Applied Mechanics*. 16th ed. Charles Griff and Company, 680 pp.

Rhee, D. M., and F. T. Lombardo, 2018: Improved near-surface wind speed characterization using damage patterns. *J. Wind Eng. Ind. Aerodyn.*, **180**, 288–297, https://doi.org/10.1016/j.jweia.2018.07.017.

——, ——, and J. Kadowski, 2021: Semi-automated tree-fall pattern identification using image processing technique: Application to Alonsa, MB tornado. *J. Wind Eng. Ind. Aerodyn.*, **208**, 104399, https://doi.org/10.1016/j.jweia.2020.104399.

Ryzhkov, A. V., T. J. Schuur, D. W. Burgess, and D. S. Zrnic, 2005: Polarimetric tornado detection. *J. Appl. Meteor.*, **44**, 557–570, https://doi.org/10.1175/JAM2235.1.

Satrio, M. A., D. J. Bodine, A. E. Reinhart, T. Maruyama, and F. T. Lombardo, 2020: Understanding how complex terrain impacts tornado dynamics using a suite of high-resolution numerical simulations. *J. Atmos. Sci.*, **77**, 3277–3300, https://doi.org/10.1175/JAS-D-19-0321.1.

Schelleng, J. C., C. R. Burrows, and E. B. Ferrell, 1933: Ultra-short-wave propagation. *Proc. IRE*, **21**, 427–463, https://doi.org/10.1109/JRPROC.1933.227639.

Schultz, C. J., and Coauthors, 2012: Dual-polarization tornadic debris signatures. Part I: Examples and utility in an operational setting. *Electron. J. Oper. Meteor.*, **13**, 120–137, http://nwafiles.nwas.org/ej/pdf/2012-EJ9.pdf.

Skow, K. D., and C. Cogil, 2017: A high-resolution aerial survey and radar analysis of quasi-linear convective system surface vortex damage paths from 31 August 2014. *Wea. Forecasting*, **32**, 441–467, https://doi.org/10.1175/WAF-D-16-0136.1.

Smith, B. T., R. L. Thompson, A. R. Dean, and P. T. Marsh, 2015: Diagnosing the conditional probability of tornado damage rating using environmental and radar attributes. *Wea. Forecasting*, **30**, 914–932, https://doi.org/10.1175/WAF-D-14-00122.1.

——, ——, D. A. Speheger, A. R. Dean, C. D. Karstens, and A. K. Anderson-Frey, 2020a: WSR-88D tornado intensity estimates. Part I: Real-time probabilities of peak tornado wind speeds. *Wea. Forecasting*, **35**, 2479–2492, https://doi.org/10.1175/WAF-D-20-0010.1.

——, ——, ——, ——, ——, and ——, 2020b: WSR-88D tornado intensity estimates. Part II: Real-time applications to tornado warning time scales. *Wea. Forecasting*, **35**, 2493–2506, https://doi.org/10.1175/WAF-D-20-0011.1.

Snyder, J. C., and H. B. Bluestein, 2014: Some considerations for the use of high-resolution mobile radar data in tornado intensity determination. *Wea. Forecasting*, **29**, 799–827, https://doi.org/10.1175/WAF-D-14-00026.1.

——, ——, Z. B. Wienhoff, C. M. Kuster, and D. W. Reif, 2020: An analysis of an ostensible anticyclonic tornado from 9 May 2016 using high-resolution, rapid-scan radar data. *Wea. Forecasting*, **35**, 1685–1712, https://doi.org/10.1175/WAF-D-20-0055.1.

Strader, S. M., and W. S. Ashley, 2018: Finescale assessment of mobile home tornado vulnerability in the central and southeast United States. *Wea. Climate Soc.*, **10**, 797–812, https://doi.org/10.1175/WCAS-D-18-0060.1.

Thompson, R. L., and Coauthors, 2017: Tornado damage rating probabilities derived from WSR-88D data. *Wea. Forecasting*, **32**, 1509–1528, https://doi.org/10.1175/WAF-D-17-0004.1.

Tanamachi, R. L., H. B. Bluestein, W.-C. Lee, M. Bell, and A. Pazmany, 2007: Ground-Based Velocity Track Display (GBVTD) analysis of W-band Doppler radar data in a tornado near Stockton, Kansas, on 15 May 1999. *Mon. Wea. Rev.*, **135**, 783–800, https://doi.org/10.1175/MWR3325.1.

——, ——, M. Xue, W.-C. Lee, K. A. Orzel, S. J. Frazier, and R. M. Wakimoto, 2013: Near-surface vortex structure in a tornado and in a sub-tornado-strength convective-storm vortex observed by a mobile, W-band radar during VORTEX2. *Mon. Wea. Rev.*, **141**, 3661–3690, https://doi.org/10.1175/MWR-D-12-00331.1.

Van Den Broeke, M. S., 2015: Polarimetric tornadic debris signature variability and debris fallout signatures. *J. Appl. Meteor. Climatol.*, **54**, 2389–2405, https://doi.org/10.1175/JAMC-D-15-0077.1.

——, and S. T. Jauernic, 2014: Spatial and temporal characteristics of polarimetric tornadic debris signatures. *J. Appl. Meteor. Climatol.*, **53**, 2217–2231, https://doi.org/10.1175/JAMC-D-14-0094.1.

Vaughan, O. H., Jr., and B. Vonnegut, 1976: Luminous electrical phenomena in Huntsville, Alabama, tornadoes on April 3, 1974. NASA Tech. Memo. NASA TM X-73301, 37 pp.,

https://ntrs.nasa.gov/api/citations/19760020697/downloads/19760020697.pdf.

Wakimoto, R. M., N. T. Atkins, and J. Wurman, 2011: The La-Grange tornado during VORTEX2. Part I: Photogrammetric analysis of the tornado combined with single-Doppler radar data. *Mon. Wea. Rev.*, **139**, 2233–2258, https://doi.org/10.1175/2010MWR3568.1.

——, P. Stauffer, W.-C. Lee, N. T. Atkins, and J. Wurman, 2012: Finescale structure of the LaGrange, Wyoming, tornado during VORTEX2: GBVTD and photogrammetric analyses. *Mon. Wea. Rev.*, **140**, 3397–3418, https://doi.org/10.1175/MWR-D-12-00036.1.

——, and Coauthors, 2016: Aerial damage survey of the 2013 El Reno tornado combined with mobile radar data. *Mon. Wea. Rev.*, **144**, 1749–1776, https://doi.org/10.1175/MWR-D-15-0367.1.

——, Z. Wienhoff, H. B. Bluestein, and D. Reif, 2018: The Dodge City tornadoes on 24 May 2016: Damage survey, photogrammetric analysis combined with mobile polarimetric radar data. *Mon. Wea. Rev.*, **146**, 3735–3771, https://doi.org/10.1175/MWR-D-18-0125.1.

——, ——, ——, D. J. Bodine, and J. M. Kurdzo, 2020: Mobile radar observations of the evolving debris field compared with a damage survey of the Shawnee, Oklahoma, tornado of 19 May 2013. *Mon. Wea. Rev.*, **148**, 1779–1803, https://doi.org/10.1175/MWR-D-19-0215.1.

Wienhoff, Z. B., H. B. Bluestein, D. W. Reif, R. M. Wakimoto, L. J. Wicker, and J. M. Kurdzo, 2020: Analysis of debris signature characteristics and evolution in the 24 May 2016 Dodge City, Kansas, tornadoes. *Mon. Wea. Rev.*, **148**, 5063–5086, https://doi.org/10.1175/MWR-D-20-0162.1.

Wieringa, J., 1980: Representativeness of wind observations at airports. *Bull. Amer. Meteor. Soc.*, **61**, 962–971, https://doi.org/10.1175/1520-0477(1980)061<0962:ROWOAA>2.0.CO;2.

Wood, V. T., R. A. Brown, and D. C. Dowell, 2009: Simulated WSR-88D velocity and reflectivity signatures of numerically modeled tornadoes. *J. Atmos. Oceanic Technol.*, **26**, 876–893, https://doi.org/10.1175/2008JTECHA1181.1.

WSEC, 2006: A recommendation for an Enhanced Fujita scale (EF-scale). Wind Science and Engineering Center, Texas Tech University, 111 pp., http://www.depts.ttu.edu/nwi/Pubs/EnhancedFujitaScale/EFScale.pdf.

Wurman, J., 2002: The multiple-vortex structure of a tornado. *Wea. Forecasting*, **17**, 473–505, https://doi.org/10.1175/1520-0434(2002)017<0473:TMVSOA>2.0.CO;2.

——, and S. Gill, 2000: Finescale radar observations of the Dimmitt, Texas (2 June 1995), tornado. *Mon. Wea. Rev.*, **128**, 2135–2164, https://doi.org/10.1175/1520-0493(2000)128<2135:FROOTD>2.0.CO;2.

——, and C. Alexander, 2005: The 30 May 1998 Spencer, South Dakota, storm. Part II: Comparison of observed damage and radar-derived winds in the tornadoes. *Mon. Wea. Rev.*, **133**, 97–119, https://doi.org/10.1175/MWR-2856.1.

——, and K. Kosiba, 2013: Finescale radar observations of tornado and mesocyclone structures. *Wea. Forecasting*, **28**, 1157–1174, https://doi.org/10.1175/WAF-D-12-00127.1.

——, Y. Richardson, C. Alexander, S. Weygandt, and P. F. Zhang, 2007a: Dual-Doppler and single-Doppler analysis of a tornadic storm undergoing mergers and repeated tornadogenesis. *Mon. Wea. Rev.*, **135**, 736–758, https://doi.org/10.1175/MWR3276.1.

——, ——, ——, ——, and ——, 2007b: Dual-Doppler analysis of winds and vorticity budget terms near a tornado. *Mon. Wea. Rev.*, **135**, 2392–2405, https://doi.org/10.1175/MWR3404.1.

——, K. Kosiba, P. Markowski, Y. Richardson, D. Dowell, and P. Robinson, 2010: Finescale single- and dual-Doppler analysis of tornado intensification, maintenance, and dissipation in the Orleans, Nebraska, supercell. *Mon. Wea. Rev.*, **138**, 4439–4455, https://doi.org/10.1175/2010MWR3330.1.

——, ——, and P. Robinson, 2013: In situ, Doppler radar, and video observations of the interior structure of a tornado and the wind–damage relationship. *Bull. Amer. Meteor. Soc.*, **94**, 835–846, https://doi.org/10.1175/BAMS-D-12-00114.1.

——, ——, ——, and T. Marshall, 2014: The role of multiple-vortex tornado structure in causing storm researcher fatalities. *Bull. Amer. Meteor. Soc.*, **95**, 31–45, https://doi.org/10.1175/BAMS-D-13-00221.1.